

RESEARCH ARTICLE

Stress-hybrid virtual element method on quadrilateral meshes for compressible and nearly-incompressible linear elasticity

Alvin Chen¹ | N. Sukumar^{*,2}

¹Department of Mathematics, University of California, Davis, CA 95616, USA

²Department of Civil and Environmental Engineering, University of California, Davis, CA 95616, USA

Correspondence

*N. Sukumar, Department of Civil and Environmental Engineering, University of California, One Shields Avenue, Davis, CA 95616, USA
Email: nsukumar@ucdavis.edu

In this paper, we propose a robust low-order stabilization-free virtual element method on quadrilateral meshes for linear elasticity that is based on the stress-hybrid principle. We refer to this approach as the Stress-Hybrid Virtual Element Method (SH-VEM). In this method, the Hellinger–Reissner variational principle is adopted, wherein both the equilibrium equations and the strain-displacement relations are variationally enforced. We consider small-strain deformations of linear elastic solids in the compressible and near-incompressible regimes over quadrilateral (convex and nonconvex) meshes. Within an element, the displacement field is approximated as a linear combination of canonical shape functions that are *virtual*. The stress field, similar to the stress-hybrid finite element method of Pian and Sumihara, is represented using a linear combination of symmetric tensor polynomials. A 5-parameter expansion of the stress field is used in each element, with stress transformation equations applied on distorted quadrilaterals. In the variational statement of the strain-displacement relations, the divergence theorem is invoked to express the stress coefficients in terms of the nodal displacements. This results in a formulation with solely the nodal displacements as unknowns. Numerical results are presented for several benchmark problems from linear elasticity. We show that SH-VEM is free of volumetric and shear locking, and it converges optimally in the L^2 norm and energy seminorm of the displacement field, and in the L^2 norm of the hydrostatic stress.

KEYWORDS:

stabilization-free virtual element method; Hellinger–Reissner variational principle; complementary strain energy; nonconvex quadrilateral; volumetric locking; shear locking

1 | INTRODUCTION

Finite element formulations that are robust (do not suffer from volumetric and shear locking) for solid continua remain a long-standing problem in computational mechanics.¹ Low-order, fully integrated displacement-based finite elements are prone to

volumetric locking as the Poisson's ratio $\nu \rightarrow 0.5$, and for bending-dominated problems, spurious shear strains (element tends to be overly stiff) lead to shear locking phenomenon. The advent of the virtual element method^{2,3} has provided new routes to potentially alleviate locking for nearly-incompressible materials. Initially, mixed variational principles, hybrid formulations, B-bar and selective reduced integration strategies that are prominent in finite element formulations for constrained problems have been adopted in the virtual element method.^{4,5,6,7,8} More recently, in the spirit of assumed-strain methods,^{9,10} projections onto higher order strains have been pursued in the VEM to devise stabilization-free schemes.^{11,12,13,14,15} In this paper, as a point of departure, we appeal to the Hellinger–Reissner variational principle and assumed stress (referred to as hybrid stress or stress hybrid) techniques^{16,17} to devise a virtual element formulation that is robust for compressible and nearly-incompressible linear elasticity over quadrilateral meshes. We refer to this approach as the Stress-Hybrid Virtual Element Method (SH-VEM).

Stress-hybrid finite element methods can be traced to the seminal work of Pian and Sumihara.¹⁶ The relationship of this approach to the method of incompatible modes¹⁸ has been established.^{19,20} Furthermore, limit principles exist that reveal the connections of finite elements that are based on the Hellinger–Reissner (two-field) and the Hu–Washizu (three-field) variational principles.²¹ In the stress-hybrid finite element approach, the displacement field and the stress field are independent. The displacement field is conforming and the stress field (discontinuous) is approximated by a linear combination of symmetric tensor polynomials on the biunit square (parent element). Since a quadrilateral element has eight displacement degrees of freedom and three rigid-body modes, a minimum of five parameters are needed for the stress approximation.¹⁶ On the parent element, the stress field is approximated using a five-term expansion (referred to as 5β), and the isoparametric map is used to obtain the expressions for the stress field in the physical xy -coordinate system. The equilibrium equations and strain-displacement relations are variationally enforced, and in so doing, the stress coefficients can be expressed in terms of the nodal displacements. This leads to a displacement formulation that solely contains nodal displacements as unknowns. Belytschko and Bindeman²² have shown that for linear problems, the stress-hybrid finite element method produces more accurate results than many assumed-strain and hourglass stabilized methods. Barlow²³ provides a rationale for the improved accuracy that the stress-hybrid method delivers by proving via a minimization principle that it is an optimal compromise between the displacement-based (stiffness) and stress-based (flexibility) formulations. For nearly-incompressible problems, the finite element method based on the former is stiff, whereas use of the latter tends to be overly flexible. There have been many different approaches within the stress-hybrid finite element method to find the best choice of stress expansion to ensure good accuracy and robustness. Several studies^{17,24,25,26} select a judicious choice of the stress expansion so that spurious zero-energy modes are excluded. Alternative approaches by Xie and Zhou^{27,28} and Cen et al.²⁹ have used energy compatibility arguments to derive the stress expansion. Jog^{30,31} has provided rules for choosing the stress functions and has extended the stress-hybrid approach to higher order elements. Xue et al.³² provide a necessary inf-sup condition to ensure the stability of stress-hybrid methods, and Zhou and Xie³³ and Yu et al.³⁴ have

analyzed the convergence of these methods. Simo et al.³⁵ showed the excellent performance of the stress formulation for linear shell theory and Simo et al.³⁶ have applied the approach for small-strain elastoplasticity. However, very few studies have explored the stress-hybrid method for nonlinear computations. Notable among them are the contributions of Jog and coworkers,^{37,38,39,40,41} who have successfully extended the stress-hybrid finite element formulation to nonlinear and inelastic analysis of solid continua, plates and shells.

In this paper, we adopt the stress-hybrid principle using a five-parameter expansion of the stress field to construct a robust stabilization-free virtual element method for plane elasticity on quadrilateral (convex and nonconvex) meshes that is free of volumetric and shear locking. On a quadrilateral, a linear symmetric tensor polynomial for a higher order strain field (nine parameters) is used in the stabilization-free virtual element method (SF-VEM),¹³ which proves to be overly stiff and suffers from volumetric locking for nearly-incompressible materials. The SH-VEM proposed herein overcomes this limitation of the SF-VEM.

The remainder of this paper is structured as follows. In Section 2, we introduce the model problem of linear elasticity and construct a weak formulation from the Hellinger–Reissner variational principle. In Section 3, we present the virtual element space and construct the required projection operators for the SH-VEM. As a point of distinction from the stress-hybrid finite element method, in the SH-VEM we use a 5β expansion of the stress field in a rotated coordinate system for distorted quadrilaterals,^{42,43} and then the stress transformation equations are used to transform them to Cartesian coordinates. Furthermore, we then invoke the divergence theorem over the distorted element (since the basis functions in the VEM are *virtual*) to express the stress coefficients in terms of the nodal displacements. In Section 4, the numerical implementation of the projection operators and the stiffness matrix is given. In Section 5, we first present numerical results for standard VEM,³ stabilization-free VEM,¹³ B-bar VEM⁶ and SH-VEM for a manufactured problem with Poisson’s ratio $\nu \in [0.3, 0.5)$. Subsequently, results are presented for B-bar VEM and SH-VEM on a series of benchmark problems for ν close to 0.5: thin cantilever beam (to demonstrate absence of shear locking), Cook’s membrane under shear end load, infinite plate with a hole under uniaxial tension, hollow pressurized cylinder and flat punch. Our main finding from this study are summarized in Section 6.

2 | HELLINGER–REISSNER VARIATIONAL FORMULATION

Consider an elastic body that occupies the region $\Omega \subset \mathbb{R}^2$ with boundary $\partial\Omega$. We assume that the boundary can be written as a disjoint union $\partial\Omega = \Gamma_u \cup \Gamma_t$ with $\Gamma_u \cap \Gamma_t = \emptyset$. Displacement boundary conditions $\mathbf{u} = \mathbf{u}_0$ are prescribed on Γ_u and tractions $\mathbf{t} = \bar{\mathbf{t}}$ are imposed on Γ_t . Let \mathbf{u} denote the displacement field, $\boldsymbol{\epsilon} = \nabla_s \mathbf{u}$ (∇_s is the symmetric gradient operator) is the small-strain tensor, $\boldsymbol{\sigma}$ is the Cauchy stress tensor, and $\mathbf{b} \in [L^2(\Omega)]^2$ is the body force per volume.

To construct the weak form, we start from the Hellinger–Reissner functional for linear elasticity, which is given by:

$$\Pi_{\text{HR}}[\mathbf{u}, \boldsymbol{\sigma}] = -\frac{1}{2} \int_{\Omega} \boldsymbol{\sigma} : \mathbb{C}^{-1} : \boldsymbol{\sigma} \, d\mathbf{x} + \int_{\Omega} \boldsymbol{\sigma} : \nabla_s \mathbf{u} \, d\mathbf{x} - \int_{\Omega} \mathbf{b} \cdot \mathbf{u} \, d\mathbf{x} - \int_{\Gamma_t} \bar{\mathbf{t}} \cdot \mathbf{u} \, ds.$$

On taking the first variation of $\Pi_{\text{HR}}(\cdot, \cdot)$ and requiring it to be stationary, we obtain

$$\delta \Pi_{\text{HR}}[\mathbf{u}, \boldsymbol{\sigma}; \delta \mathbf{u}, \delta \boldsymbol{\sigma}] = \int_{\Omega} \delta \boldsymbol{\sigma} : (\nabla_s \mathbf{u} - \mathbb{C}^{-1} : \boldsymbol{\sigma}) \, d\mathbf{x} + \int_{\Omega} \boldsymbol{\sigma} : \nabla_s (\delta \mathbf{u}) \, d\mathbf{x} - \int_{\Omega} \mathbf{b} \cdot \delta \mathbf{u} \, d\mathbf{x} - \int_{\Gamma_t} \bar{\mathbf{t}} \cdot \delta \mathbf{u} \, ds = 0 \quad \forall \delta \mathbf{u} \in \mathcal{V}_u, \delta \boldsymbol{\sigma} \in \mathcal{V}_\sigma,$$

where \mathcal{V}_u contains vector-valued functions in the Hilbert space $[H^1(\Omega)]^2$ that also vanish on Γ_u , whereas \mathcal{V}_σ contains functions in $(L^2)_{\text{sym}}^{2 \times 2}$. This gives us the weak statement of the equilibrium equations and strain-displacement relations:

$$\int_{\Omega} \boldsymbol{\sigma} : \nabla_s (\delta \mathbf{u}) \, d\mathbf{x} - \int_{\Omega} \mathbf{b} \cdot \delta \mathbf{u} \, d\mathbf{x} - \int_{\Gamma_t} \bar{\mathbf{t}} \cdot \delta \mathbf{u} \, ds = 0 \quad \forall \delta \mathbf{u} \in \mathcal{V}_u, \quad (1a)$$

$$\int_{\Omega} \delta \boldsymbol{\sigma} : (\nabla_s \mathbf{u} - \mathbb{C}^{-1} : \boldsymbol{\sigma}) \, d\mathbf{x} = 0 \quad \forall \delta \boldsymbol{\sigma} \in \mathcal{V}_\sigma. \quad (1b)$$

3 | VIRTUAL ELEMENT DISCRETIZATION

Let \mathcal{T}^h be a decomposition of Ω into nonoverlapping quadrilaterals. For each quadrilateral $E \in \mathcal{T}^h$, let h_E denote its diameter, \mathbf{x}_E its centroid, and $\mathbf{x}_i = (x_i, y_i)$ the coordinate of the i -th vertex.

3.1 | Polynomial basis

In the virtual element method, we need a polynomial approximation space for the displacement field. For each element E , define $[\mathbb{P}_1(E)]^2$ as the space of two-dimensional vector-valued polynomials of degree less than or equal to one. For this space, we choose a basis of scaled vector monomials given by:

$$\widehat{\mathbf{M}}(E) = \left[\begin{bmatrix} 1 \\ 0 \end{bmatrix}, \begin{bmatrix} 0 \\ 1 \end{bmatrix}, \begin{bmatrix} -\eta \\ \xi \end{bmatrix}, \begin{bmatrix} \eta \\ \xi \end{bmatrix}, \begin{bmatrix} \xi \\ 0 \end{bmatrix}, \begin{bmatrix} 0 \\ \eta \end{bmatrix} \right], \quad (2a)$$

where

$$\xi = \frac{x - x_E}{h_E}, \quad \eta = \frac{y - y_E}{h_E}. \quad (2b)$$

We denote the α -th vector of $\widehat{\mathbf{M}}(E)$ by \mathbf{m}_α . We also need to define an approximation space for the stress field. Using Voigt representation, we define a basis for the space $[\mathbb{P}_1(E)]_{\text{sym}}^{2 \times 2}$ of 2×2 symmetric polynomials of degree less than or equal to one:

$$\widehat{\mathbf{M}}^{2 \times 2}(E) = \left[\begin{array}{c} \left\{ \begin{array}{c} 1 \\ 0 \\ 0 \end{array} \right\}, \left\{ \begin{array}{c} 0 \\ 1 \\ 0 \end{array} \right\}, \left\{ \begin{array}{c} 0 \\ 0 \\ 1 \end{array} \right\}, \left\{ \begin{array}{c} \xi \\ 0 \\ 0 \end{array} \right\}, \left\{ \begin{array}{c} 0 \\ \xi \\ 0 \end{array} \right\}, \left\{ \begin{array}{c} 0 \\ 0 \\ \xi \end{array} \right\}, \left\{ \begin{array}{c} \eta \\ 0 \\ 0 \end{array} \right\}, \left\{ \begin{array}{c} 0 \\ \eta \\ 0 \end{array} \right\}, \left\{ \begin{array}{c} 0 \\ 0 \\ \eta \end{array} \right\} \end{array} \right].$$

3.2 | Energy projection of the displacement field

We first define the energy projection of the displacement field from standard virtual element formulations. For each element E , define $\Pi^\epsilon : [H^1(E)]^2 \rightarrow [\mathbb{P}_1(E)]^2$ as a function that satisfies the orthogonality relation:

$$\int_E \boldsymbol{\varepsilon}(\mathbf{m}_\alpha) : \mathbb{C} : \boldsymbol{\varepsilon}(\mathbf{v} - \Pi^\epsilon \mathbf{v}) d\mathbf{x} = 0 \quad \forall \mathbf{m}_\alpha \in \widehat{\mathbf{M}}(E). \quad (3)$$

We note that $\boldsymbol{\varepsilon}(\mathbf{m}_\alpha) = \mathbf{0}$ for $\alpha = 1, 2, 3$, since these \mathbf{m}_α correspond to rigid-body modes. Therefore, we obtain three trivial equations $0 = 0$. In order to define a unique projection, we choose a projection operator $P_0 : [H^1(E)]^2 \times [H^1(E)]^2 \rightarrow \mathbb{R}$ to replace these three trivial equations. In particular, we choose a discrete L^2 inner product:

$$P_0(\mathbf{u}, \mathbf{v}) = \frac{1}{4} \sum_{k=1}^4 \mathbf{u}(\mathbf{x}_k) \cdot \mathbf{v}(\mathbf{x}_k), \quad (4a)$$

and require three additional conditions:

$$P_0(\mathbf{m}_\alpha, \mathbf{v} - \Pi^\epsilon \mathbf{v}) = \frac{1}{4} \sum_{k=1}^4 \mathbf{m}_\alpha(\mathbf{x}_k) \cdot (\mathbf{v} - \Pi^\epsilon \mathbf{v})(\mathbf{x}_k) = 0 \quad (\alpha = 1, 2, 3). \quad (4b)$$

Now we define the energy projection $\Pi^\epsilon \mathbf{v}$ as the unique function that satisfies the following two relations:

$$\frac{1}{4} \sum_{k=1}^4 \mathbf{m}_\alpha(\mathbf{x}_k) \cdot (\mathbf{v} - \Pi^\epsilon \mathbf{v})(\mathbf{x}_k) = 0 \quad (\alpha = 1, 2, 3), \quad (5a)$$

$$\int_E \boldsymbol{\varepsilon}(\mathbf{m}_\alpha) : \mathbb{C} : \boldsymbol{\varepsilon}(\mathbf{v} - \Pi^\epsilon \mathbf{v}) d\mathbf{x} = 0 \quad (\alpha = 4, 5, 6). \quad (5b)$$

Following Chen and Sukumar,¹³ we write (5b) in matrix-vector form as

$$\int_E (\mathbf{S} \Pi^\epsilon \mathbf{v})^T (\mathbf{C} \mathbf{S} \mathbf{m}_\alpha) d\mathbf{x} = \int_E (\mathbf{S} \mathbf{v})^T (\mathbf{C} \mathbf{S} \mathbf{m}_\alpha) d\mathbf{x}, \quad (6a)$$

$$\mathbf{S} = \begin{bmatrix} \frac{\partial}{\partial x} & 0 \\ 0 & \frac{\partial}{\partial y} \\ \frac{\partial}{\partial y} & \frac{\partial}{\partial x} \end{bmatrix}, \quad \mathbf{C} = \frac{E_Y}{(1+\nu)(1-2\nu)} \begin{bmatrix} 1-\nu & \nu & 0 \\ \nu & 1-\nu & 0 \\ 0 & 0 & \frac{1-2\nu}{2} \end{bmatrix}, \quad (6b)$$

where \mathbf{C} is the matrix representation (plane strain) of the material moduli tensor, and E_Y and ν are the Young's modulus and Poisson's ratio, respectively, of the material.

3.3 | Stress-hybrid projection operator

We now define the projection operator for the stress-hybrid formulation. On choosing $\delta\boldsymbol{\sigma} = \mathbb{P} \in [\mathbb{P}_1(E)]_{\text{sym}}^{2 \times 2}$ and $\boldsymbol{\sigma} \in [\mathbb{P}_1(E)]_{\text{sym}}^{2 \times 2}$ in (1b), we have

$$\int_{\Omega} \mathbb{P} : (\nabla_s \mathbf{u} - \mathbb{C}^{-1} : \boldsymbol{\sigma}) \, d\mathbf{x} = 0.$$

This condition is true for all $\mathbb{P} \in [\mathbb{P}_1(E)]_{\text{sym}}^{2 \times 2}$, so we can view $\mathbb{C}^{-1} : \boldsymbol{\sigma}$ as a projection of $\nabla_s \mathbf{u}$ with respect to the space $[\mathbb{P}_1(E)]_{\text{sym}}^{2 \times 2}$. Now, let the assumed stress field be taken as $\boldsymbol{\sigma} := \Pi_{\beta} \boldsymbol{\sigma}$, where Π_{β} is the stress projection operator. Then, the orthogonality condition becomes

$$\int_E \mathbb{P} : (\nabla_s \mathbf{u} - \mathbb{C}^{-1} : \Pi_{\beta} \boldsymbol{\sigma}) \, d\mathbf{x} = 0 \quad \forall \mathbb{P} \in [\mathbb{P}_1(E)]_{\text{sym}}^{2 \times 2},$$

or equivalently

$$\int_E \mathbb{P} : \mathbb{C}^{-1} : \Pi_{\beta} \boldsymbol{\sigma} \, d\mathbf{x} = \int_E \mathbb{P} : \nabla_s \mathbf{u} \, d\mathbf{x} \quad \forall \mathbb{P} \in [\mathbb{P}_1(E)]_{\text{sym}}^{2 \times 2}.$$

After applying the divergence theorem and simplifying, we obtain

$$\int_E \mathbb{P} : \mathbb{C}^{-1} : \Pi_{\beta} \boldsymbol{\sigma} \, d\mathbf{x} = \int_{\partial E} (\mathbb{P} \cdot \mathbf{n}) \cdot \mathbf{u} \, ds - \int_E (\nabla \cdot \mathbb{P}) \cdot \mathbf{u} \, d\mathbf{x}, \quad (8)$$

where $\mathbf{n} = (n_x, n_y)^T$ is the outward unit normal along ∂E . For later implementation, we convert this expression into the associated matrix-vector form. Let $\overline{\mathbb{P}}, \overline{\Pi_{\beta} \boldsymbol{\sigma}}$ be the Voigt representation of \mathbb{P} and $\Pi_{\beta} \boldsymbol{\sigma}$, respectively. Then, (8) can be written as

$$\int_E \overline{\mathbb{P}}^T \mathbf{C}^{-1} \overline{\Pi_{\beta} \boldsymbol{\sigma}} \, d\mathbf{x} = \int_{\partial E} \overline{\mathbb{P}}^T \mathbf{N}^{\partial E} \mathbf{u} \, ds - \int_E (\partial \overline{\mathbb{P}})^T \mathbf{u} \, d\mathbf{x} \quad \forall \mathbb{P} \in [\mathbb{P}_1(E)]_{\text{sym}}^{2 \times 2}, \quad (9a)$$

where $\mathbf{N}^{\partial E}$ is the representation of the outward normals and ∂ is the matrix divergence operator that are given by

$$\mathbf{N}^{\partial E} := \begin{bmatrix} n_x & 0 \\ 0 & n_y \\ n_y & n_x \end{bmatrix}, \quad \partial := \begin{bmatrix} \frac{\partial}{\partial x} & 0 & \frac{\partial}{\partial y} \\ 0 & \frac{\partial}{\partial y} & \frac{\partial}{\partial x} \end{bmatrix}. \quad (9b)$$

4 | NUMERICAL IMPLEMENTATION

4.1 | Virtual element space

We define the first order vector-valued virtual element space on an element E as:^{2,44}

$$\mathbf{V}(E) = \left\{ \mathbf{v}_h \in [H^1(E)]^2 : \Delta \mathbf{v}_h \in [\mathbb{P}_1(E)]^2, \mathbf{v}_h|_e \in [\mathbb{P}_1(e)]^2 \forall e \in \partial E, \mathbf{v}_h|_{\partial E} \in [C^0(\partial E)]^2, \right. \\ \left. \int_E \mathbf{v}_h \cdot \mathbf{p} \, d\mathbf{x} = \int_E \Pi^\epsilon \mathbf{v}_h \cdot \mathbf{p} \, d\mathbf{x} \quad \forall \mathbf{p} \in [\mathbb{P}_1(E)]^2 \right\}. \quad (10)$$

On this space, the functions are affine along each edge, so we can choose the degrees of freedom (DOFs) to be the function values at the vertices of E . Each element has a total of eight displacement DOFs. For each element E we also assign a basis for the local space $\mathbf{V}(E)$. Let $\{\phi_i\}$ be the standard scalar basis functions in standard VEM² that satisfy the property $\phi_i(\mathbf{x}_j) = \delta_{ij}$.

Using the scalar basis, we define the matrix of vector-valued basis functions by

$$\boldsymbol{\varphi} = \begin{bmatrix} \phi_1 & \phi_2 & \phi_3 & \phi_4 & 0 & 0 & 0 & 0 \\ 0 & 0 & 0 & 0 & \phi_1 & \phi_2 & \phi_3 & \phi_4 \end{bmatrix} := \begin{bmatrix} \boldsymbol{\varphi}_1 & \boldsymbol{\varphi}_2 & \dots & \boldsymbol{\varphi}_8 \end{bmatrix}, \quad (11a)$$

then any function $\mathbf{v}_h \in \mathbf{V}(E)$ can be represented as:

$$\mathbf{v}_h(\mathbf{x}) = \sum_{i=1}^8 \boldsymbol{\varphi}_i(\mathbf{x}) v_i = \boldsymbol{\varphi} \mathbf{d}, \quad (11b)$$

where v_i is the i -th degree of freedom of \mathbf{v}_h .

4.2 | Matrix representation of the energy projection

To construct the energy projection of the displacement on the virtual element space $\mathbf{V}(E)$, we follow the construction in Chen and Sukumar.¹³ Let $\mathbf{v}_h = \boldsymbol{\varphi}_i$ be the i -th basis function ($i = 1, 2, \dots, 8$), then substituting into (5a) and (6a), we obtain:

$$\frac{1}{4} \sum_{k=1}^4 \mathbf{m}_\alpha(\mathbf{x}_k) \cdot \Pi^\epsilon \boldsymbol{\varphi}_i(\mathbf{x}_k) = \frac{1}{4} \sum_{k=1}^4 \mathbf{m}_\alpha(\mathbf{x}_k) \cdot \boldsymbol{\varphi}_i(\mathbf{x}_k) \quad (\alpha = 1, 2, 3), \quad (12a)$$

$$\int_E (\mathbf{S} \Pi^\epsilon \boldsymbol{\varphi}_i)^T (\mathbf{C} \mathbf{S} \mathbf{m}_\alpha) \, d\mathbf{x} = \int_E (\mathbf{S} \boldsymbol{\varphi}_i)^T (\mathbf{C} \mathbf{S} \mathbf{m}_\alpha) \, d\mathbf{x} \quad (\alpha = 4, 5, 6). \quad (12b)$$

The projection $\Pi^\epsilon \boldsymbol{\varphi}_i$ is a linear vector polynomial, therefore we expand it in terms of the basis in (2a). That is:

$$\Pi^\epsilon \boldsymbol{\varphi}_i = \sum_{\mu=1}^6 s_\mu^i \mathbf{m}_\mu := \sum_{\mu=1}^6 (\Pi_*^\epsilon)_{\mu i} \mathbf{m}_\mu \quad (i = 1, 2, \dots, 8).$$

After substituting in (12) and simplifying, we obtain the energy projection coefficients Π_*^ϵ as¹³

$$\Pi_*^\epsilon = \mathbf{G}^{-1} \mathbf{B}, \quad (13a)$$

where for $\mu = 1, 2, \dots, 6$

$$\mathbf{G}_{\alpha\mu} = \begin{cases} \frac{1}{4} \sum_{j=1}^4 \mathbf{m}_\mu(\mathbf{x}_j) \cdot \mathbf{m}_\alpha(\mathbf{x}_j) & (\alpha = 1, 2, 3) \\ \int_E (\mathbf{S}\mathbf{m}_\mu)^T (\mathbf{C}\mathbf{S}\mathbf{m}_\alpha) d\mathbf{x} & (\alpha = 4, 5, 6), \end{cases} \quad (13b)$$

and for $i = 1, 2, \dots, 8$

$$\mathbf{B}_{\alpha i} = \begin{cases} \frac{1}{4} \sum_{j=1}^4 \boldsymbol{\varphi}_i(\mathbf{x}_j) \cdot \mathbf{m}_\alpha(\mathbf{x}_j) & (\alpha = 1, 2, 3) \\ \int_E (\mathbf{S}\boldsymbol{\varphi}_i)^T (\mathbf{C}\mathbf{S}\mathbf{m}_\alpha) d\mathbf{x} & (\alpha = 4, 5, 6). \end{cases} \quad (13c)$$

The matrix $\mathbf{\Pi}_*^\epsilon$ is the coefficients of the energy projection with respect to the polynomial basis $\widehat{\mathbf{M}}(E)$. For later implementation of the B-bar VEM, it is convenient to define the coefficients with respect to the basis functions $\boldsymbol{\varphi}$. Let \mathbf{D} be the matrix of DOFs of vectors in $\widehat{\mathbf{M}}(E)$, which is given by

$$\mathbf{D} = \begin{bmatrix} \mathbf{m}_1(\mathbf{x}_1) & \mathbf{m}_2(\mathbf{x}_1) & \dots & \mathbf{m}_6(\mathbf{x}_1) \\ \mathbf{m}_1(\mathbf{x}_2) & \mathbf{m}_2(\mathbf{x}_2) & \dots & \mathbf{m}_6(\mathbf{x}_2) \\ \dots & \dots & \dots & \dots \\ \mathbf{m}_1(\mathbf{x}_4) & \mathbf{m}_2(\mathbf{x}_4) & \dots & \mathbf{m}_6(\mathbf{x}_4) \end{bmatrix}. \quad (14)$$

Then the representation of the energy projection with respect to the basis functions $\boldsymbol{\varphi}$ is:⁴⁵

$$\mathbf{\Pi}^\epsilon := \mathbf{D}\mathbf{\Pi}_*^\epsilon. \quad (15)$$

4.3 | Matrix representation of the stress-hybrid projection

We present the matrix representation of the SH-VEM projection, which relies on the rotated coordinates introduced by Cook⁴² (see Figure 1). In the SH-VEM, an assumed stress ansatz is first defined on E' (rotated element) and then transformed to E using the stress transformation equations. The computation of the element stiffness matrix is carried out on E .

4.3.1 | Rotated coordinates

It is known that using global Cartesian coordinates to construct a 5-term expansion of the stress field leads to an incomplete stress approximation and the resulting element stiffness matrix is not rotationally invariant.^{16,42,46} We follow the modification proposed by Cook⁴² to construct a local coordinate system for each element E . Let $\mathbf{x}_P, \mathbf{x}_Q, \mathbf{x}_R, \mathbf{x}_S$ be the midpoints of the edges of element E (see Figure 1). Define L_1 and L_2 as the length of the line segments PQ and RS , respectively. Then, we compute

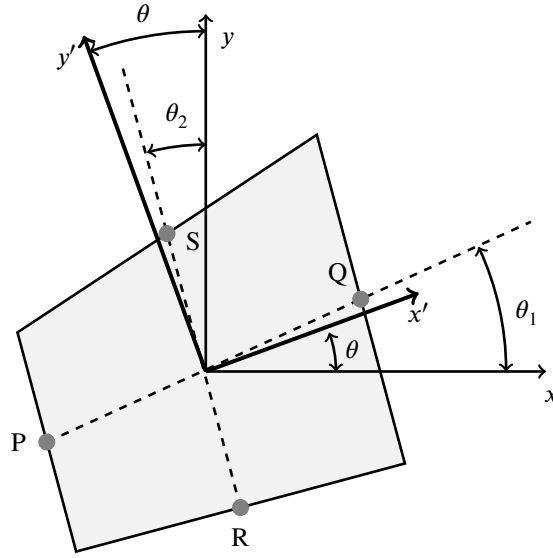


FIGURE 1 Construction of the local coordinate system for a distorted quadrilateral.

the angles

$$\theta_1 = \arctan\left(\frac{y_Q - y_P}{x_Q - x_P}\right), \quad \theta_2 = \arctan\left(\frac{x_R - x_S}{y_S - y_R}\right), \quad \theta = \frac{L_1\theta_1 + L_2\theta_2}{L_1 + L_2}. \quad (16)$$

On using the angle θ , we define the rotated coordinates (x', y') via the transformation

$$\mathbf{x}' := \begin{Bmatrix} x' \\ y' \end{Bmatrix} = \begin{bmatrix} c & s \\ -s & c \end{bmatrix} \begin{Bmatrix} x \\ y \end{Bmatrix} := \mathbf{Q}\mathbf{x}, \quad c = \cos \theta, \quad s = \sin \theta. \quad (17)$$

4.3.2 | Stress-hybrid virtual element formulation

We now present the stress-hybrid approach, which constructs the stress basis functions and stiffness matrix over the distorted element E . On a square, the selection of the stress basis in the stress-hybrid finite element method as¹⁶

$$\mathbf{M}_{5\beta} = \left[\begin{Bmatrix} 1 \\ 0 \\ 0 \end{Bmatrix}, \begin{Bmatrix} 0 \\ 1 \\ 0 \end{Bmatrix}, \begin{Bmatrix} 0 \\ 0 \\ 1 \end{Bmatrix}, \begin{Bmatrix} y \\ 0 \\ 0 \end{Bmatrix}, \begin{Bmatrix} 0 \\ 0 \\ x \end{Bmatrix} \right]$$

ensures that uniform stress states as well as pure bending can be exactly represented. To tailor this approach to VEM, we use this 5β stress expansion in a local coordinate system (E is rotated) and then apply the stress transformation equations to obtain the stress ansatz on E .

Let E' be the rotated element with vertices (x'_i, y'_i) , centroid $\mathbf{x}'_{E'}$ and diameter $h'_{E'}$. In a rotated element E' , we assume the stress expansion $\overline{\Pi_\beta \sigma'} = \mathbf{P}' \boldsymbol{\beta}'$, where \mathbf{P}' is given by

$$\mathbf{P}' = \begin{bmatrix} 1 & 0 & 0 & \eta' & 0 \\ 0 & 1 & 0 & 0 & \xi' \\ 0 & 0 & 1 & 0 & 0 \end{bmatrix} = \begin{bmatrix} \mathbf{P}'_1 & \mathbf{P}'_2 & \mathbf{P}'_3 & \mathbf{P}'_4 & \mathbf{P}'_5 \end{bmatrix}, \quad (18a)$$

and the rotated scaled monomials are

$$\xi' = \frac{x' - x'_{E'}}{h'_{E'}}, \quad \eta' = \frac{y' - y'_{E'}}{h'_{E'}}. \quad (18b)$$

On viewing each column \mathbf{P}'_i of the matrix \mathbf{P}' as an equivalent tensor \mathbf{P}'_i , we apply the rotation matrix \mathbf{Q} given in (17) to obtain a transformed tensor \mathbf{P}_i :

$$\mathbf{P}_i = \mathbf{Q}^T \mathbf{P}'_i \mathbf{Q}. \quad (19)$$

After computing each tensor \mathbf{P}_i and rewriting them in terms of 3×1 vectors \mathbf{P}_i , we define the matrix \mathbf{P}^* by⁴²

$$\mathbf{P}^* = \begin{bmatrix} \mathbf{P}_1 & \mathbf{P}_2 & \mathbf{P}_3 & \mathbf{P}_4 & \mathbf{P}_5 \end{bmatrix} = \begin{bmatrix} c^2 & s^2 & -2cs & c^2(c\eta - s\xi) & s^2(c\xi + s\eta) \\ s^2 & c^2 & 2cs & s^2(c\eta - s\xi) & c^2(c\xi + s\eta) \\ cs & -cs & c^2 - s^2 & cs(c\eta - s\xi) & -cs(c\xi + s\eta) \end{bmatrix}, \quad (20)$$

where c and s are given in (17). Without loss of generality, we choose an orthogonal basis for terms representing constant stresses, which results in the matrix

$$\mathbf{P} = \begin{bmatrix} 1 & 0 & 0 & c^2(c\eta - s\xi) & s^2(c\xi + s\eta) \\ 0 & 1 & 0 & s^2(c\eta - s\xi) & c^2(c\xi + s\eta) \\ 0 & 0 & 1 & cs(c\eta - s\xi) & -cs(c\xi + s\eta) \end{bmatrix}. \quad (21)$$

We now construct the stress-hybrid projection operator on the space $\mathbf{V}(E)$ over the original element E with respect to the basis \mathbf{P} . From (9a), we have the relation:

$$\int_E \overline{\mathbb{P}}^T \mathbf{C}^{-1} \overline{\Pi_\beta \sigma} d\mathbf{x} = \int_{\partial E} \overline{\mathbb{P}}^T \mathbf{N}^{\partial E} \mathbf{u}_h ds - \int_E \left(\partial \overline{\mathbb{P}} \right)^T \mathbf{u}_h d\mathbf{x}.$$

Expanding \mathbf{u}_h in terms of the basis in $\mathbf{V}(E)$, we have $\mathbf{u}_h = \boldsymbol{\varphi} \mathbf{d}$, where \mathbf{d} is the displacement vector. We also expand $\overline{\Pi_\beta \sigma}$ in terms of \mathbf{P} : $\overline{\Pi_\beta \sigma} = \mathbf{P} \boldsymbol{\beta}$, and since \mathbb{P} is arbitrary we take $\overline{\mathbb{P}} = \mathbf{P}_i$ ($i = 1, 2, \dots, 5$). After substituting in (9a) for each $i = 1, 2, \dots, 5$ and simplifying, we obtain the system:

$$\left(\int_E \mathbf{P}^T \mathbf{C}^{-1} \mathbf{P} d\mathbf{x} \right) \boldsymbol{\beta} = \left(\int_{\partial E} \mathbf{P}^T \mathbf{N}^{\partial E} \boldsymbol{\varphi} ds - \int_E (\partial \mathbf{P})^T \boldsymbol{\varphi} d\mathbf{x} \right) \mathbf{d}. \quad (22)$$

For this choice of \mathbf{P} , we have $\partial \mathbf{P} = \mathbf{0}$ (divergence-free), so we obtain

$$\left(\int_E \mathbf{P}^T \mathbf{C}^{-1} \mathbf{P} d\mathbf{x} \right) \boldsymbol{\beta} = \left(\int_{\partial E} \mathbf{P}^T \mathbf{N}^{\partial E} \boldsymbol{\varphi} ds \right) \mathbf{d}. \quad (23)$$

Now define the corresponding matrices \mathbf{H} and \mathbf{L} by

$$\mathbf{H} = \int_E \mathbf{P}^T \mathbf{C}^{-1} \mathbf{P} d\mathbf{x}, \quad \mathbf{L} = \int_{\partial E} \mathbf{P}^T \mathbf{N}^{\partial E} \boldsymbol{\varphi} ds, \quad (24a)$$

and then the stress coefficients are given by

$$\boldsymbol{\beta} = \mathbf{H}^{-1} \mathbf{L} \mathbf{d} := \boldsymbol{\Pi}_\beta \mathbf{d}, \quad (24b)$$

where $\boldsymbol{\Pi}_\beta$ is the matrix representation of the stress-hybrid projection operator with respect to the symmetric tensor polynomial basis \mathbf{P} .

4.4 | Element stiffness matrix and element force vector

Following the structure of (1a), we define the discrete system using the projection operator $\boldsymbol{\Pi}_\beta \boldsymbol{\sigma}$ by:

$$a_h^E(\mathbf{u}_h, \delta \mathbf{u}_h) = \ell_h^E(\delta \mathbf{u}_h),$$

where

$$\begin{aligned} a_h^E(\mathbf{u}_h, \delta \mathbf{u}_h) &:= \int_E \overline{\boldsymbol{\Pi}_\beta \boldsymbol{\sigma}(\delta \mathbf{u}_h)}^T \mathbf{C}^{-1} \overline{\boldsymbol{\Pi}_\beta \boldsymbol{\sigma}(\mathbf{u}_h)} d\mathbf{x}, \\ \ell_h^E(\delta \mathbf{u}_h) &:= \int_E (\delta \mathbf{u}_h)^T \mathbf{b} d\mathbf{x} + \int_{\Gamma_i \cap \partial E} (\delta \mathbf{u}_h)^T \bar{\mathbf{t}} ds. \end{aligned}$$

Expanding $\overline{\boldsymbol{\Pi}_\beta \boldsymbol{\sigma}}$ in terms of $\boldsymbol{\beta}$ and applying (24b), we obtain

$$a_h^E(\mathbf{u}_h, \delta \mathbf{u}_h) = (\delta \mathbf{d})^T (\boldsymbol{\Pi}_\beta)^T \left(\int_E \mathbf{P}^T \mathbf{C}^{-1} \mathbf{P} d\mathbf{x} \right) \boldsymbol{\Pi}_\beta \mathbf{d} := (\delta \mathbf{d})^T \mathbf{K}_E \mathbf{d}, \quad (26)$$

where we identify the element stiffness matrix for SH-VEM as

$$\mathbf{K}_E = (\boldsymbol{\Pi}_\beta)^T \left(\int_E \mathbf{P}^T \mathbf{C}^{-1} \mathbf{P} d\mathbf{x} \right) \boldsymbol{\Pi}_\beta = \boldsymbol{\Pi}_\beta^T \mathbf{H} \boldsymbol{\Pi}_\beta. \quad (27)$$

In the Appendix, we give an alternate stress-hybrid virtual element formulation based on Cook's approach,⁴² and show that it is identical to the stress-hybrid element stiffness matrix that is obtained using \mathbf{P}^* in (20).

Now for every element E , the element force vector is given by

$$\mathbf{f}_E := \int_E \boldsymbol{\varphi}^T \mathbf{b} d\mathbf{x} + \int_{\Gamma_i \cap \partial E} \boldsymbol{\varphi}^T \bar{\mathbf{t}} ds. \quad (28)$$

For a low-order method, the first term in (28) is approximated by taking the nodal average of the basis functions $\boldsymbol{\varphi}$ and then using a single-point quadrature to compute the integral.¹³ The second term is computed using Gauss quadrature over the element edges.

4.5 | B-bar VEM

For later numerical tests, we compare the results of the SH-VEM to a B-bar VEM. Following Park et al.,⁶ we first decompose the material moduli matrix \mathbf{C} in terms of its eigenvectors:

$$\mathbf{C} = \sum_{i=1}^3 \lambda_i \mathbf{p}_i \mathbf{p}_i^T, \quad (29)$$

where $(\lambda_i, \mathbf{p}_i)$ is the i -th eigenpair of \mathbf{C} . It is known for plane elasticity that $\mathbf{p}_1 = \frac{1}{\sqrt{2}}[1, 1, 0]^T$ and $\lambda_1 = 2\kappa + \frac{2\mu}{3}$, where κ is the bulk modulus and μ is the shear modulus. We express (29) as

$$\mathbf{C} = \lambda_1 \mathbf{p}_1 \mathbf{p}_1^T + \sum_{i=2}^3 \lambda_i \mathbf{p}_i \mathbf{p}_i^T := \mathbf{C}_{\text{dil}} + \mathbf{C}_{\text{dev}}. \quad (30)$$

The element stiffness matrix in the B-bar formulation is the sum of a consistency matrix and a stabilization matrix. For the consistency matrix \mathbf{K}^c , we have after simplification:

$$\begin{aligned} \mathbf{K}^c &= (\boldsymbol{\Pi}_*^\epsilon)^T \left(\int_E (\mathbf{S}\mathbf{M})^T \mathbf{C} (\mathbf{S}\mathbf{M}) d\mathbf{x} \right) \boldsymbol{\Pi}_*^\epsilon \\ &= (\boldsymbol{\Pi}_*^\epsilon)^T \left(\int_E (\mathbf{S}\mathbf{M})^T \mathbf{C}_{\text{dil}} (\mathbf{S}\mathbf{M}) d\mathbf{x} \right) \boldsymbol{\Pi}_*^\epsilon + (\boldsymbol{\Pi}_*^\epsilon)^T \left(\int_E (\mathbf{S}\mathbf{M})^T \mathbf{C}_{\text{dev}} (\mathbf{S}\mathbf{M}) d\mathbf{x} \right) \boldsymbol{\Pi}_*^\epsilon \\ &:= \mathbf{K}_{\text{dil}}^c + \mathbf{K}_{\text{dev}}^c, \end{aligned} \quad (31)$$

where \mathbf{S} is defined in (6b), $\boldsymbol{\Pi}_*^\epsilon$ is given in (13a) and \mathbf{M} is:

$$\mathbf{M} = \begin{bmatrix} 1 & 0 & -\eta & \eta & \xi & 0 \\ 0 & 1 & \xi & \xi & 0 & \eta \end{bmatrix}.$$

The expression for the stabilization matrix is:

$$\mathbf{K}^s = (\mathbf{I} - \boldsymbol{\Pi}^\epsilon)^T \boldsymbol{\Lambda} (\mathbf{I} - \boldsymbol{\Pi}^\epsilon), \quad (32a)$$

where $\mathbf{\Pi}^\epsilon$ is defined in (15) and $\mathbf{\Lambda}$ is a diagonal matrix with components

$$\Lambda_{ii} = \max \left((\mathbf{K}_{\text{dev}}^c)_{ii}, \frac{\mu}{2} \right). \quad (32b)$$

5 | NUMERICAL RESULTS

We present a collection of two-dimensional numerical examples for linear elasticity under plane strain conditions. We examine the errors of the displacements in the L^2 norm and energy seminorm, and the L^2 error of the hydrostatic stress. The exact hydrostatic stress (denoted by \tilde{p}) and its numerical approximation are computed as:

$$\tilde{p} = \frac{\text{trace}(\boldsymbol{\sigma})}{3}, \quad \tilde{p}_h = \frac{1+\nu}{3} \left(\left(\overline{\Pi_\beta \boldsymbol{\sigma}} \right)_1 + \left(\overline{\Pi_\beta \boldsymbol{\sigma}} \right)_2 \right), \quad (33)$$

where $\left(\overline{\Pi_\beta \boldsymbol{\sigma}} \right)_i$ is the i -th component of $\overline{\Pi_\beta \boldsymbol{\sigma}}$.

The convergence rates of B-bar VEM and SH-VEM are computed using the following discrete error measures:

$$\|\mathbf{u} - \mathbf{u}_h\|_{L^2(\Omega)} = \sqrt{\sum_E \int_E |\mathbf{u} - \mathbf{\Pi}^\epsilon \mathbf{u}_h|^2 d\mathbf{x}}, \quad (34a)$$

$$\|\tilde{p} - \tilde{p}_h\|_{L^2(\Omega)} = \sqrt{\sum_E \int_E |\tilde{p} - \tilde{p}_h|^2 d\mathbf{x}}, \quad (34b)$$

$$\|\mathbf{u} - \mathbf{u}_h\|_a = \sqrt{\sum_E \int_E (\boldsymbol{\sigma} - \overline{\Pi_\beta \boldsymbol{\sigma}})^T \mathbf{C}^{-1} (\boldsymbol{\sigma} - \overline{\Pi_\beta \boldsymbol{\sigma}}) d\mathbf{x}}. \quad (34c)$$

The matrix \mathbf{H} in (24a) and the integrals that appear in (34) are computed using the scaled boundary cubature scheme;⁴⁷ see also Chen and Sukumar^{13,14} for its use in the stabilization-free virtual element method.

5.1 | Eigenanalysis of the element stiffness matrix

We first examine the stability of the SH-VEM for rotated elements through an eigenanalysis. From Cook,⁴² it is known that for a noninvariant method, a rectangular element rotated by $\frac{\pi}{4}$ will contain spurious zero-energy modes. For this test, we take a unit square and rotate it by angle $\alpha = 0, \frac{\pi}{6}, \frac{\pi}{4}, \frac{\pi}{3}$, and then compute the eigenvalues of the element stiffness matrix. The material has Young's modulus $E_Y = 1$ psi and Poisson's ratio $\nu = 0.4999999$. Three formulations are considered: an unrotated 5β , rotated 5β and an unrotated 7β . In the unrotated formulations, the projection matrix is computed on the original element E without applying the rotated coordinate transformation given in (17), and for the 7β formulation a 7-term expansion is used for \mathbf{P} :

$$\mathbf{P} = \begin{bmatrix} 1 & 0 & 0 & \eta & 0 & 0 & \xi \\ 0 & 1 & 0 & 0 & \xi & \eta & 0 \\ 0 & 0 & 1 & 0 & 0 & -\xi & -\eta \end{bmatrix}.$$

Every method has three physical zero eigenvalues that correspond to the zero-energy modes. For a method to be stable the next lowest eigenvalue must be positive and not close to zero. In Table 1, we indicate the fourth smallest eigenvalue of the element stiffness matrix for the three formulations. The table shows that both the rotated 5β and the unrotated 7β have their eigenvalues unaffected for any α . However, as α is increased to $\alpha = \frac{\pi}{4}$, the next lowest eigenvalue of the unrotated 5β formulation becomes zero. This shows that the 5β SH-VEM in global coordinates is not rotationally invariant. Numerical tests also reveal that the 7β formulation ameliorates volumetric locking but is much stiffer for pure bending problems, and therefore both unrotated 5β and 7β formulations are not considered in the remainder of this paper.

Method	$\alpha = 0$	$\alpha = \frac{\pi}{6}$	$\alpha = \frac{\pi}{4}$	$\alpha = \frac{\pi}{3}$
Unrotated 5β	0.444	0.111	0.000	0.111
Rotated 5β	0.444	0.444	0.444	0.444
Unrotated 7β	0.444	0.444	0.444	0.444

TABLE 1 Comparison of the fourth-lowest eigenvalue on a square that is rotated by angle α for three stress-hybrid VEMs.

To further test the stability of the SH-VEM on different convex and nonconvex element types, we consider two additional tests. For the second test, we study the effects of perturbing a vertex of a unit square. We construct quadrilaterals with coordinates $\{(0, 0), (1, 0), (\alpha, \beta), (0, 1)\}$, where $\alpha, \beta \in (0.05, 10)$. For every combination of α and β we compute the element stiffness matrix on this quadrilateral and then determine its fourth smallest eigenvalue. A few representative elements and a contour plot of the eigenvalues are shown in Figure 2. The contour plot reveals that deviations from the unit square decreases the value of the fourth smallest eigenvalue; however, the eigenvalue remains positive and away from zero (greater than 0.003) in all cases. This test shows that no spurious zero eigenvalues appear even for large perturbations of the unit square.

In the third test, we examine the effects of varying the angles of a unit square by constructing quadrilaterals with coordinates $\{(0, 0), (\cos \alpha, -\sin \alpha), (1, 1), (-\sin \beta, \cos \beta)\}$, where $\alpha, \beta \in \left[-\frac{\pi}{4}, \frac{\pi}{2}\right]$. We again compute the eigenvalues of the element stiffness matrix for different combinations of α and β . Figure 3 shows a few representative elements and a contour plot of the fourth smallest eigenvalue. The contour plot shows that the smallest nonzero eigenvalue remains positive and away from zero (greater than 0.004) for any combination of $\alpha, \beta \in \left[-\frac{\pi}{4}, \frac{\pi}{2}\right]$, and hence demonstrates that distorting a quadrilateral by varying its angle does not affect the stability of SH-VEM.

5.2 | Manufactured problem: Convergence in the incompressible limit

We examine the effects of increasing the Poisson ratio to the incompressible limit ($\nu \rightarrow 0.5$) on a manufactured problem with a known solution.¹ The problem domain is the unit square and the Young's modulus $E_Y = 1$ psi and the Poisson's ratio

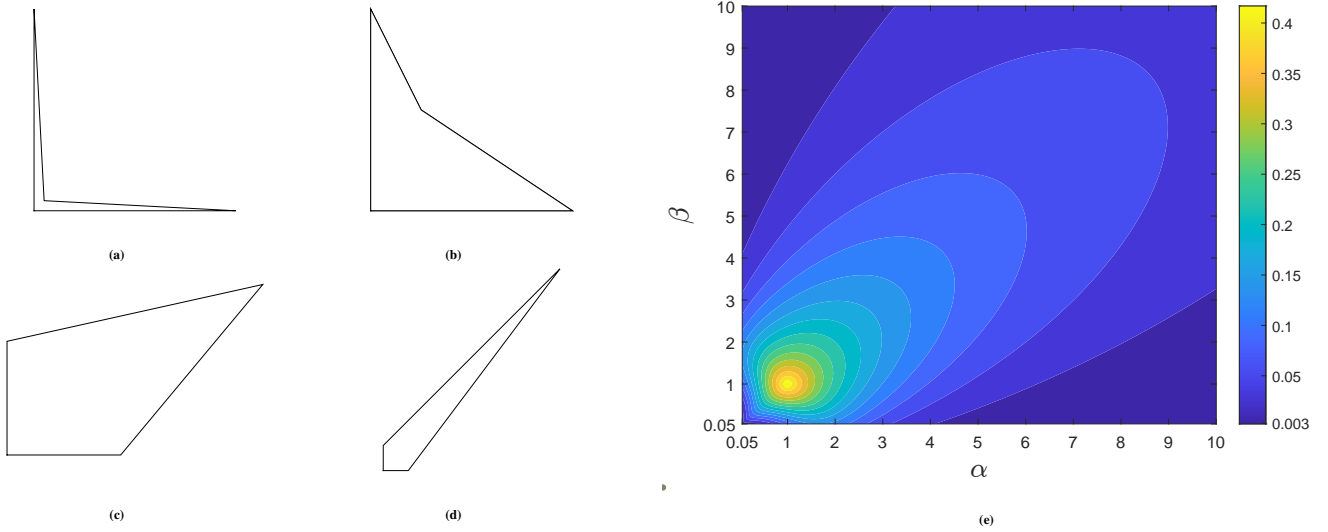


FIGURE 2 (a)–(d) First sequence of distorted quadrilaterals, where the fourth vertex is located at (α, β) , and (e) contour plot of the fourth-lowest eigenvalue as a function of α and β .

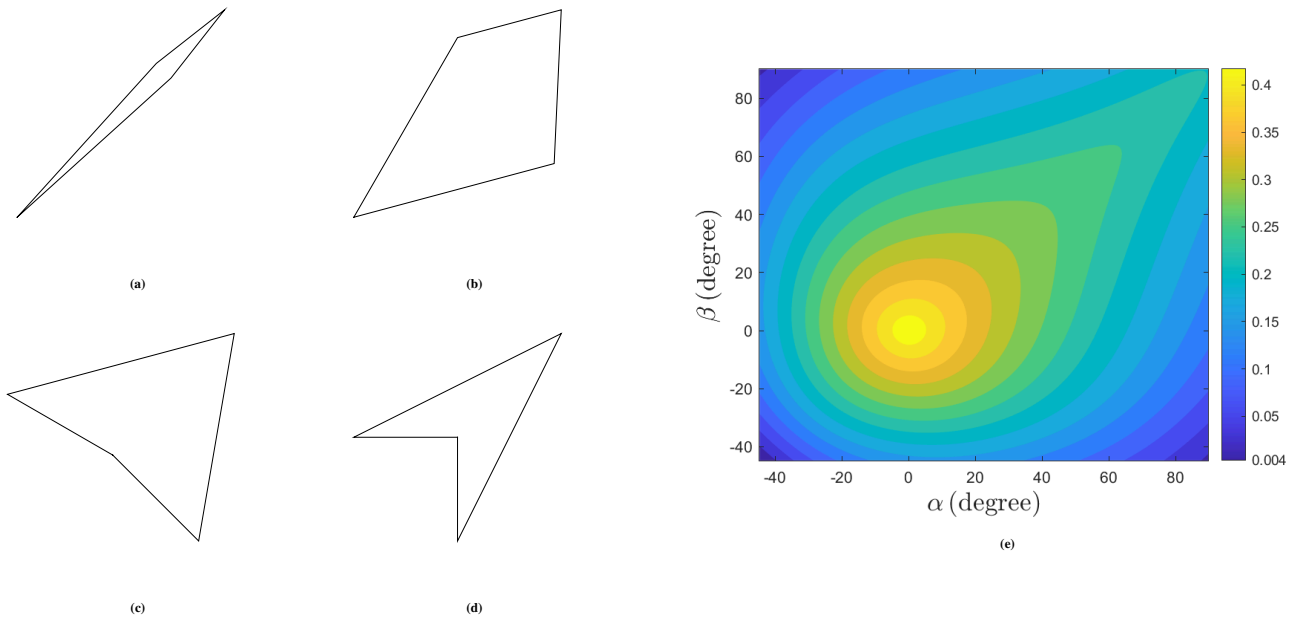


FIGURE 3 (a)–(d) Second sequence of distorted quadrilaterals, where the two vertices that are varied are located at $(\cos \alpha, -\sin \alpha)$ and $(-\sin \beta, \cos \beta)$, and (e) contour plot of the fourth-lowest eigenvalue as a function of α and β .

$\nu \in \{0.3, 0.4, 0.4999, 0.4999999\}$. The exact solution with associated loading is given by:

$$u(\mathbf{x}) = -\cos(\pi x) \sin(\pi y) \text{ and } v(\mathbf{x}) = \sin(\pi x) \cos(\pi y), \quad \mathbf{b}(\mathbf{x}) = \frac{\pi^2}{1 + \nu} \begin{Bmatrix} \cos(\pi x) \sin(\pi y) \\ -\sin(\pi x) \cos(\pi y) \end{Bmatrix}.$$

In Figure 4, we show a few sample meshes for the unit square, and in Figure 5 we show the convergence rates in L^2 error of displacement and the energy seminorm as ν is varied. We assess four formulations: standard VEM,³ SF-VEM,¹³ B-bar VEM,⁶

and SH-VEM. From these plots, we observe that as ν is increased, the standard VEM and SF-VEM fail to converge, while both B-bar VEM and SH-VEM converge with rates that are in agreement with theory.

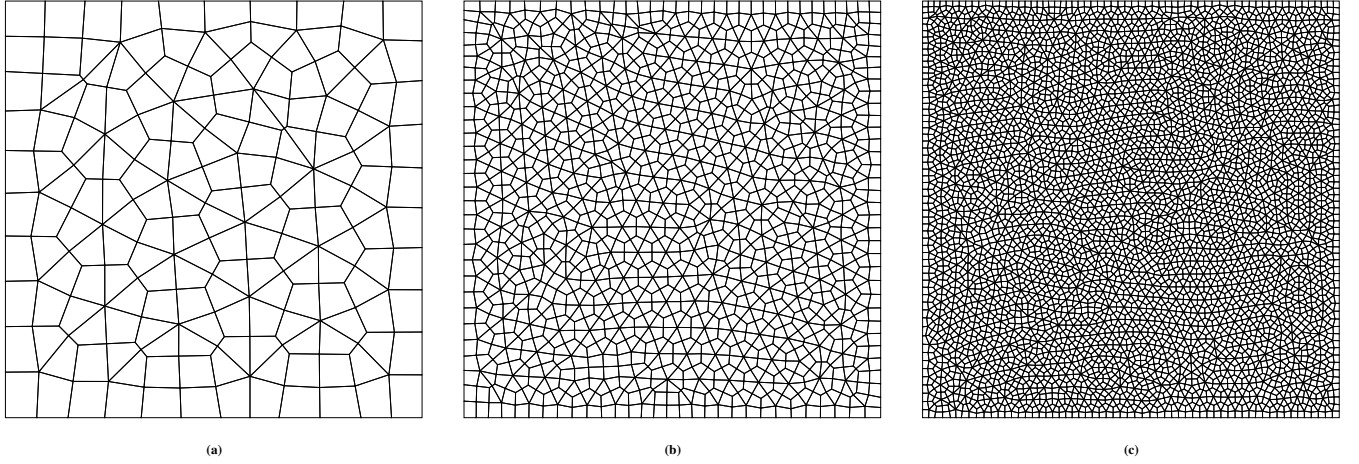


FIGURE 4 Quadrilateral meshes for the manufactured problem. (a) 150 elements, (b) 1500 elements and (c) 6000 elements.

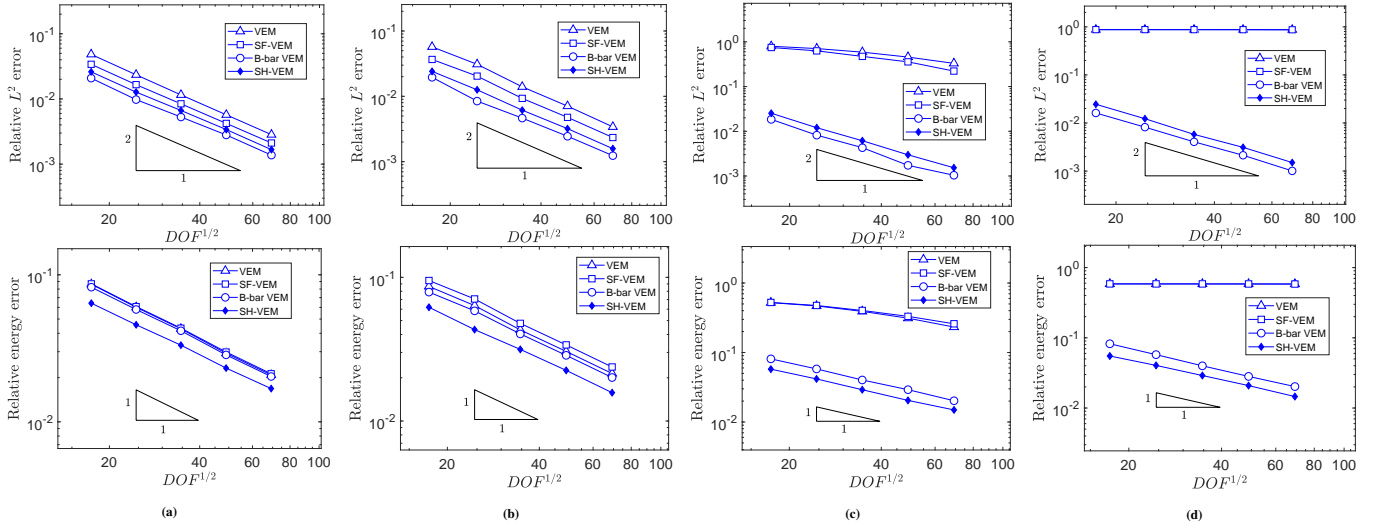


FIGURE 5 Comparison of the convergence of standard VEM, stabilization-free VEM, B-bar VEM and SH-VEM for the manufactured problem. Each column represents a different value of ν . (a) $\nu = 0.3$ and (b) $\nu = 0.4$, (c) $\nu = 0.4999$ and (d) $\nu = 0.4999999$.

We also test this problem on nonconvex meshes. We begin with a uniform rectangular mesh and then split each element into a convex and a nonconvex quadrilateral. A few sample meshes are shown in Figure 6. Numerical results are presented in Figure 7, which reveal that even on nonconvex meshes B-bar VEM and SH-VEM retain optimal rates of convergence.

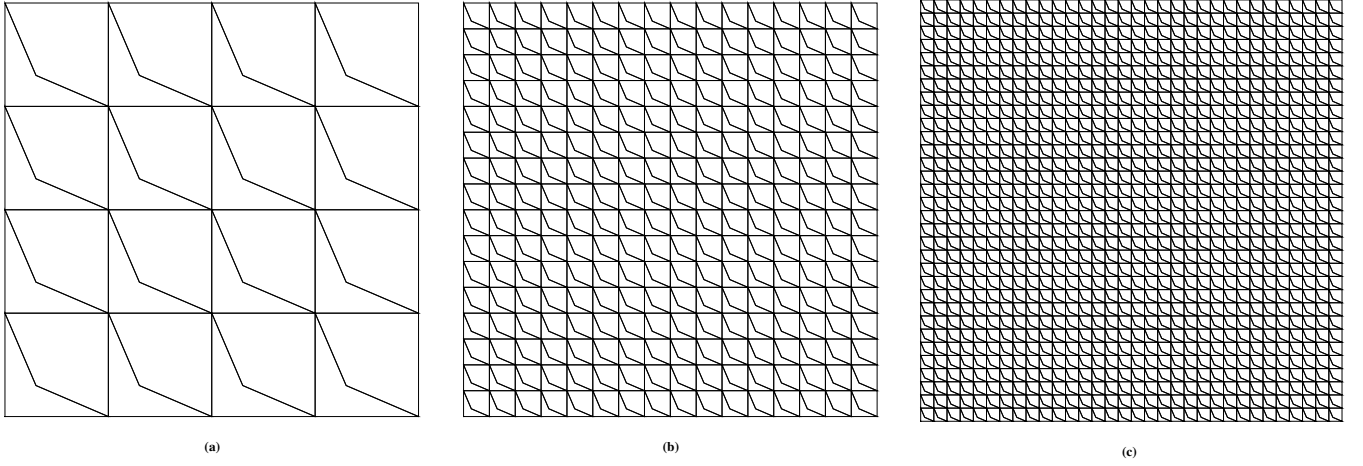


FIGURE 6 Nonconvex quadrilateral meshes for the manufactured problem. (a) 32 elements, (b) 512 elements and (c) 2048 elements.

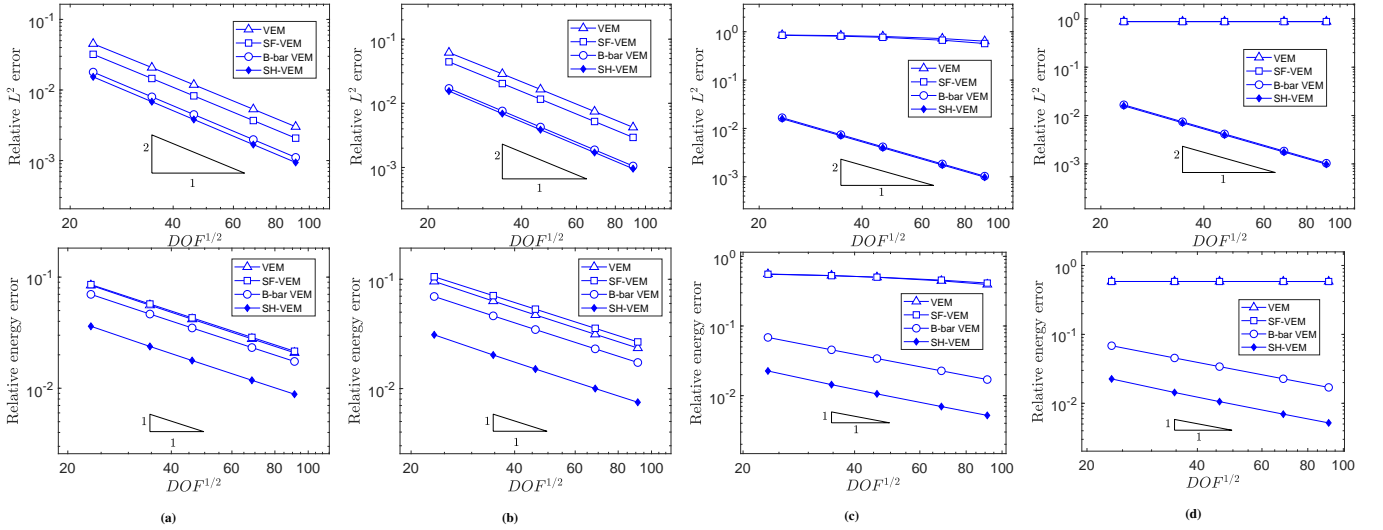


FIGURE 7 Comparison of the convergence of standard VEM, stabilization-free VEM, B-bar VEM and SH-VEM for the manufactured problem on nonconvex meshes. Each column represents a different value of ν . (a) $\nu = 0.3$ and (b) $\nu = 0.4$, (c) $\nu = 0.4999$ and (d) $\nu = 0.4999999$.

Lastly, we examine the conditioning of the global stiffness matrix to ensure that increasing the Poisson's ratio and varying the element shapes and refinement does not lead to ill-conditioning. In Figure 8, we show the condition number of the four methods as $\nu \rightarrow 0.5$ on both unstructured and nonconvex meshes. From the plot, we observe that the condition number of SH-VEM is comparable to the other three methods for compressible materials. As the material becomes nearly incompressible, the condition number increases for all methods on the coarsest mesh. However, we observe that the growth of the condition number with refinement for B-bar VEM and SH-VEM is similar to the case when $\nu = 0.3$, which is in agreement with the $\mathcal{O}(h^{-2})$ increase of the stiffness matrix condition number in the finite element method.

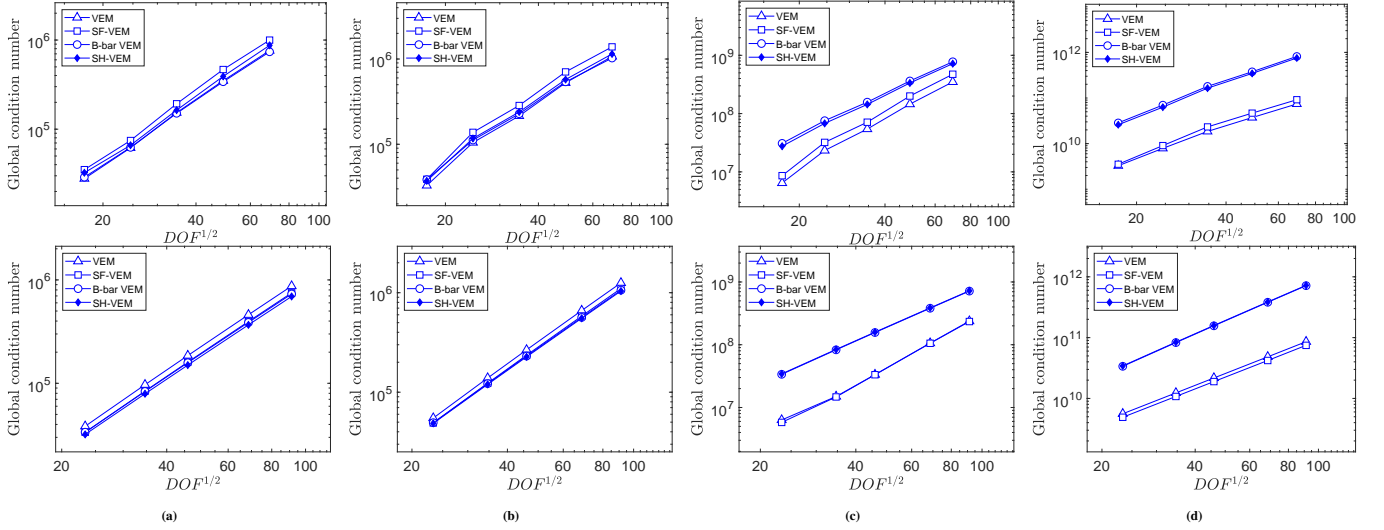


FIGURE 8 Comparison of the conditioning of the global stiffness matrix of the standard VEM, stabilization-free VEM, B-bar VEM and SH-VEM for the manufactured problem. The first row is for the unstructured quadrilateral mesh, the second row is for the nonconvex mesh. Each column represents a different value of ν . (a) $\nu = 0.3$ and (b) $\nu = 0.4$, (c) $\nu = 0.4999$ and (d) $\nu = 0.499999$.

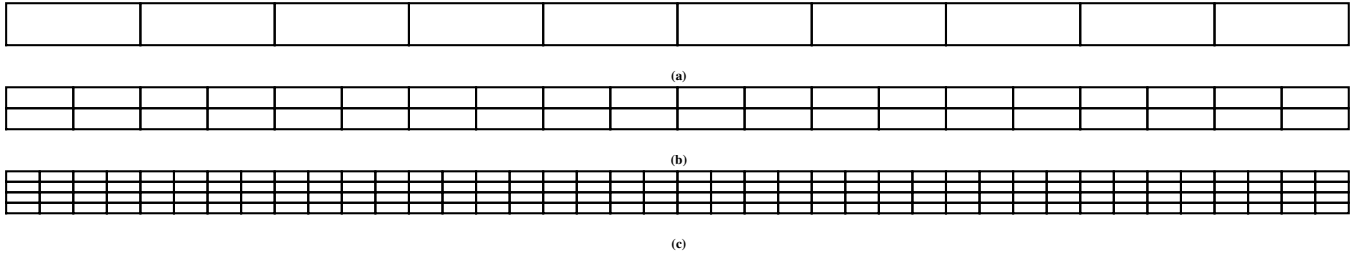


FIGURE 9 Rectangular meshes for the cantilever beam problem. (a) 10 elements, (b) 40 elements and (c) 160 elements.

5.3 | Thin cantilever beam

We consider the problem of a thin cantilever beam under a shear end load.⁴⁸ The material has Young's modulus $E_Y = 1 \times 10^5$ psi and $\nu = 0.49995$. The beam has length $L = 32$ inch, height $D = 1$ inch and unit thickness. The left boundary is fixed and a shear end load of $P = -100$ lbf is applied on the right boundary. We use a regular rectangular mesh with $N \in \{1, 2, 4, 8, 16\}$ elements along the height and $10N$ elements along the length. In Figure 9, we show a few representative meshes and in Figure 10 we compare the rates of convergence of B-bar VEM to SH-VEM in the three error norms. In Figure 11, we plot the end displacement of the three methods and contours of the hydrostatic stress for SH-VEM. From these results, we observe that the accuracy of SH-VEM is far superior to B-bar VEM and the displacements in the SH-VEM display superconvergence (close to the exact solution) on coarse rectangular meshes.

We consider another test for the cantilever beam problem using a mesh with either one or two elements along the height and M elements along the length. We choose the number of elements $M \in \{2, 4, 8, 16\}$. The meshes are depicted in Figure 12 and

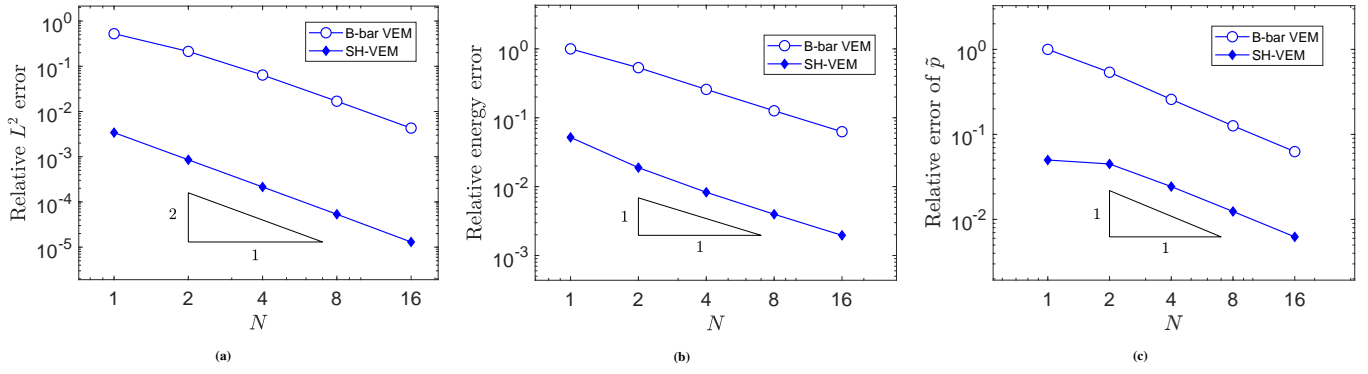


FIGURE 10 Comparison of B-bar VEM and SH-VEM for the thin cantilever beam problem. (a) L^2 error of displacement, (b) energy error and (c) L^2 error of hydrostatic stress, where N is the number of elements along the height of the beam.

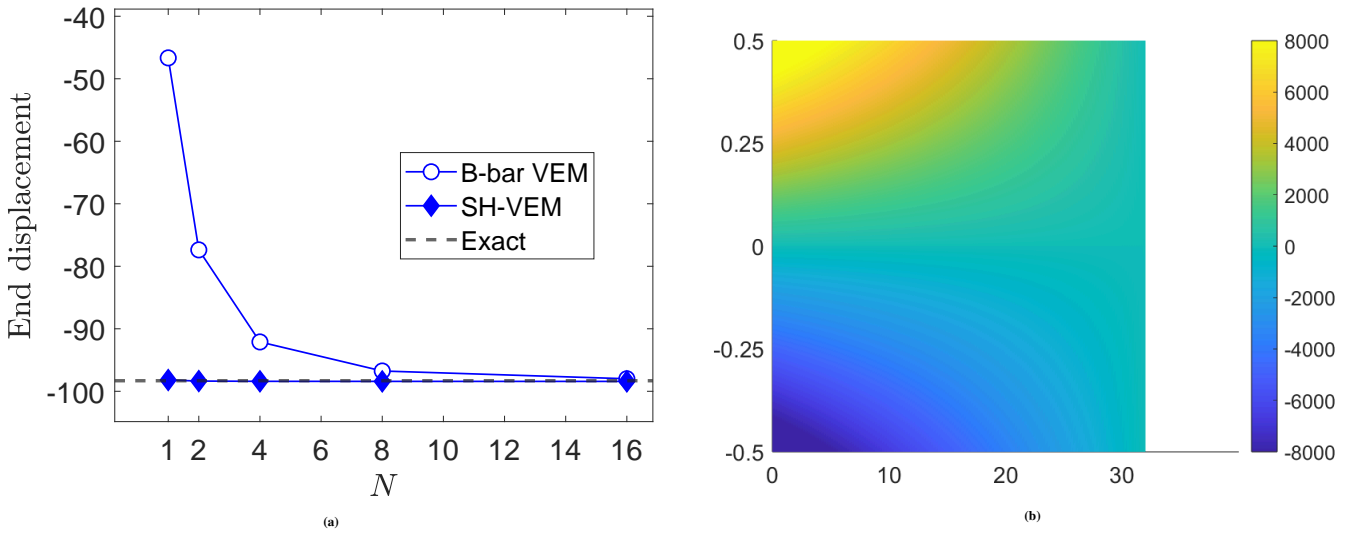


FIGURE 11 (a) Convergence of the end displacement for the cantilever beam problem. The mesh consists of $10N \times N$ rectangular elements, where N is the number of elements along the height of the beam, (b) contour plot of hydrostatic stress for SH-VEM.

the convergence of the tip displacement for the two cases is presented in Figure 13. The plots reveal that SH-VEM is accurate even for high aspect ratio elements and is free of shear locking. However, for one element along the height and with refinement along the length, we observe that B-bar VEM converges to a value below the exact value (see Figure 13a) and for the case of two elements along the height, the end displacement is not accurate (see Figure 13b).

It is known that distortions of a rectangular mesh can lead to shear locking in the thin beam problem.⁴⁹ We study this issue on perturbed trapezoidal meshes that are shown in Figure 14. In Figure 15, we present the convergence of the end displacement. The plot shows that on such meshes SH-VEM is convergent but with reduced accuracy; however, note that the B-bar formulation fails to converge to the exact end displacement for the case $N = 1$ (see Figure 15a).

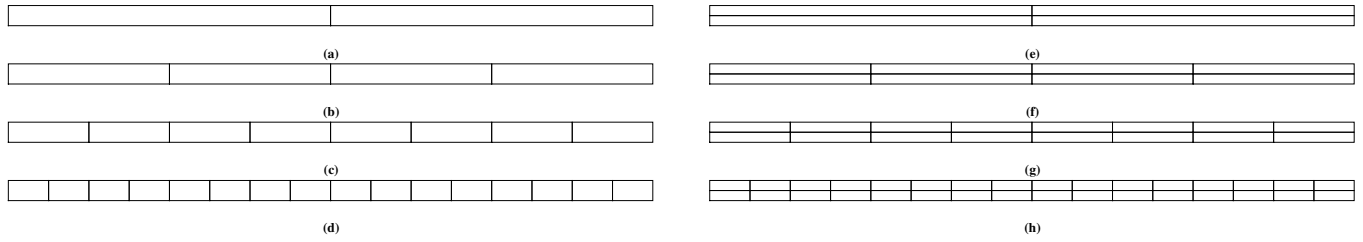


FIGURE 12 Rectangular meshes for the cantilever beam problem with fixed length to height ratio for each element. (a), (b), (c), (d) 16:1, 8:1, 4:1 and 2:1; and (e), (f), (g), (h) 32:1, 16:1, 8:1 and 4:1.

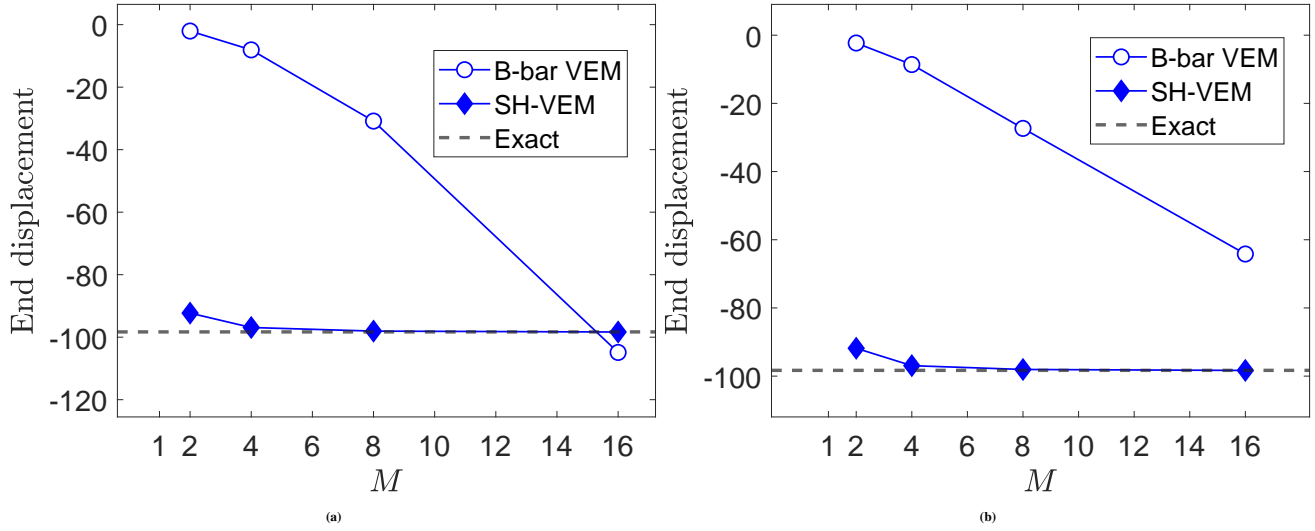


FIGURE 13 Convergence of the end displacement for the cantilever beam problem. The mesh consists of $M \times N$ quadrilaterals, where M is the number of elements along the length of the beam. (a) $N = 1$ and (b) $N = 2$.

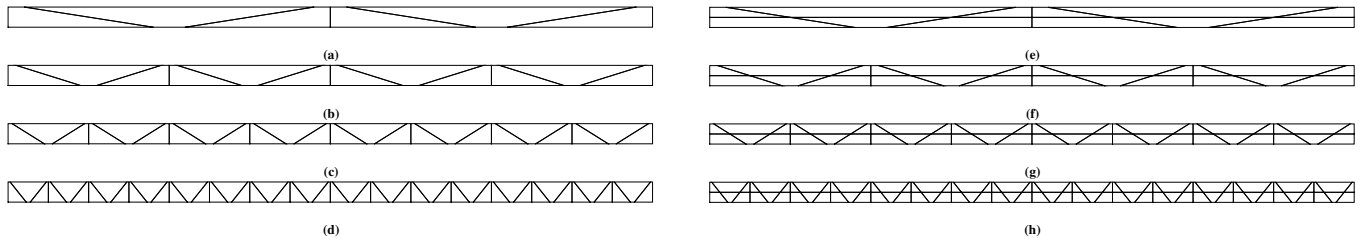


FIGURE 14 Trapezoidal meshes for the cantilever beam problem. Mesh is refined along the length with (a) 1 element along the height and (b) 2 elements along the height.

We also solve the cantilever beam problem on nearly degenerate quadrilateral meshes. We start with a regular rectangular mesh, and then split each element into four quadrilaterals with two of the elements have collapsing edges. A few sample meshes are shown in Figure 16. In Figure 17, we compare the convergence rates of B-bar VEM and SH-VEM in the three norms, and in Figure 18 we present the convergence of the tip displacement as well as the contour plot of the hydrostatic stress using SH-VEM. The plots reveal that B-bar VEM and SH-VEM retain optimal convergence rates. Furthermore, the convergence of SH-VEM is

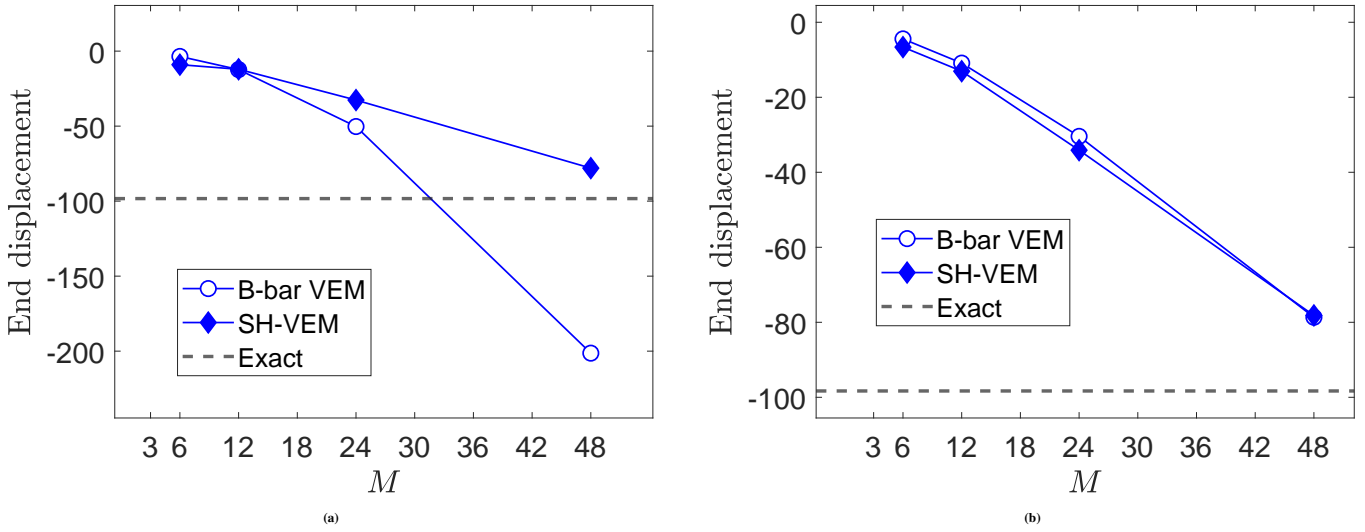


FIGURE 15 Convergence of the end displacement for the cantilever beam problem. The mesh consists of $M \times N$ trapezoids, where M is the number of elements along the length of the beam. (a) $N = 1$ and (b) $N = 2$.

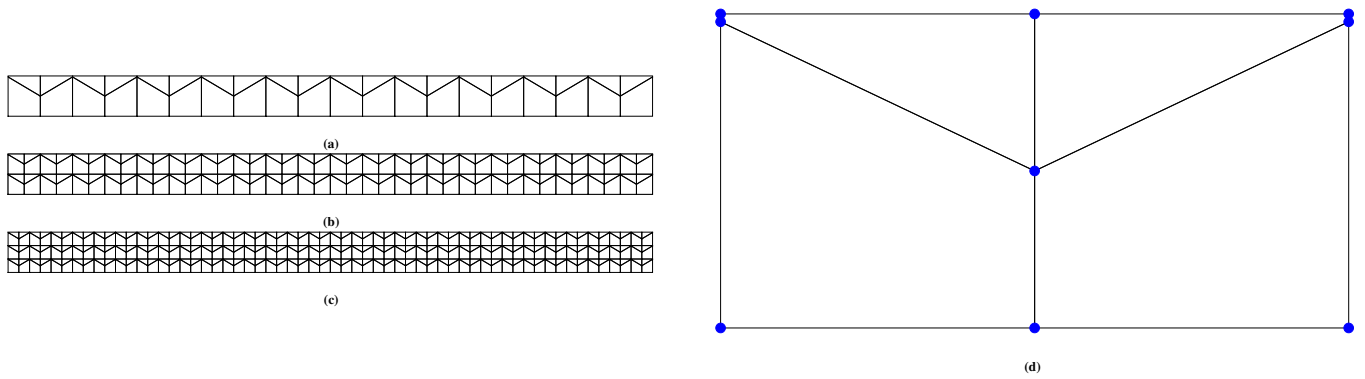


FIGURE 16 Nearly degenerate meshes used for the cantilever beam problem. (a) 40 elements, (b) 160 elements (c) 360 elements, and (d) magnification of a single element split into four quadrilaterals.

monotonic; however its accuracy is worse when compared to the uniform mesh case. This decrease in accuracy can be attributed to the poor shape (near-degeneracy) quality of the elements.

5.4 | Cook's membrane

Here we consider the Cook's membrane problem under shear load⁴² (see Figure 19). This problem is commonly used to test a combination of bending and shear for nearly-incompressible materials. The material has Young's modulus $E_Y = 250$ psi and Poisson's ratio $\nu = 0.4999999$. The left edge of the membrane is fixed and the right edge has an applied shear load of $F = 6.25$ lbf per unit length. We first test this problem on an unstructured quadrilateral mesh. A few sample meshes are shown in Figure 19. In Figure 20, the convergence of the tip displacement and that of the hydrostatic stress are presented. The plot shows that the

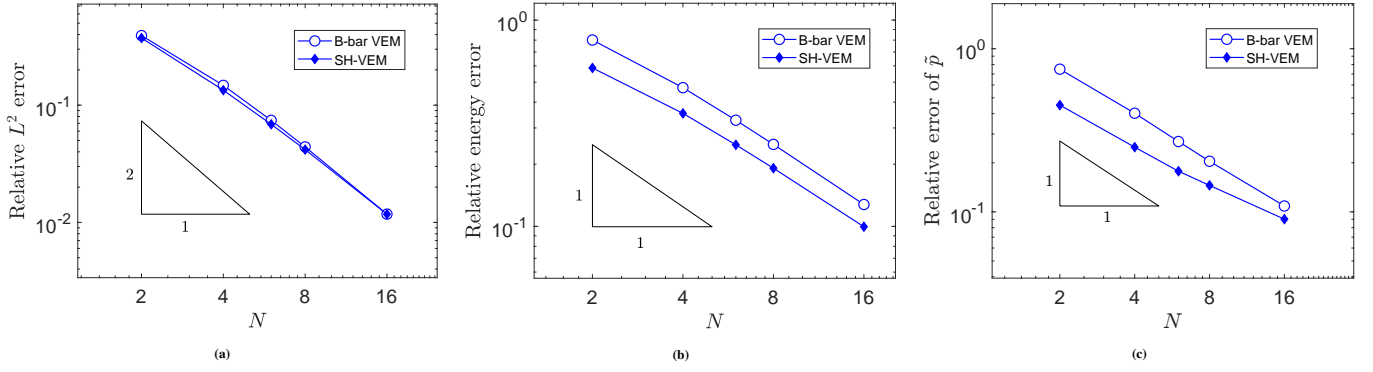


FIGURE 17 Comparison of B-bar VEM and SH-VEM for the thin cantilever beam problem on nearly degenerate meshes. (a) L^2 error of displacement, (b) energy error and (c) L^2 error of hydrostatic stress, where N is the number of elements along the height of the beam.

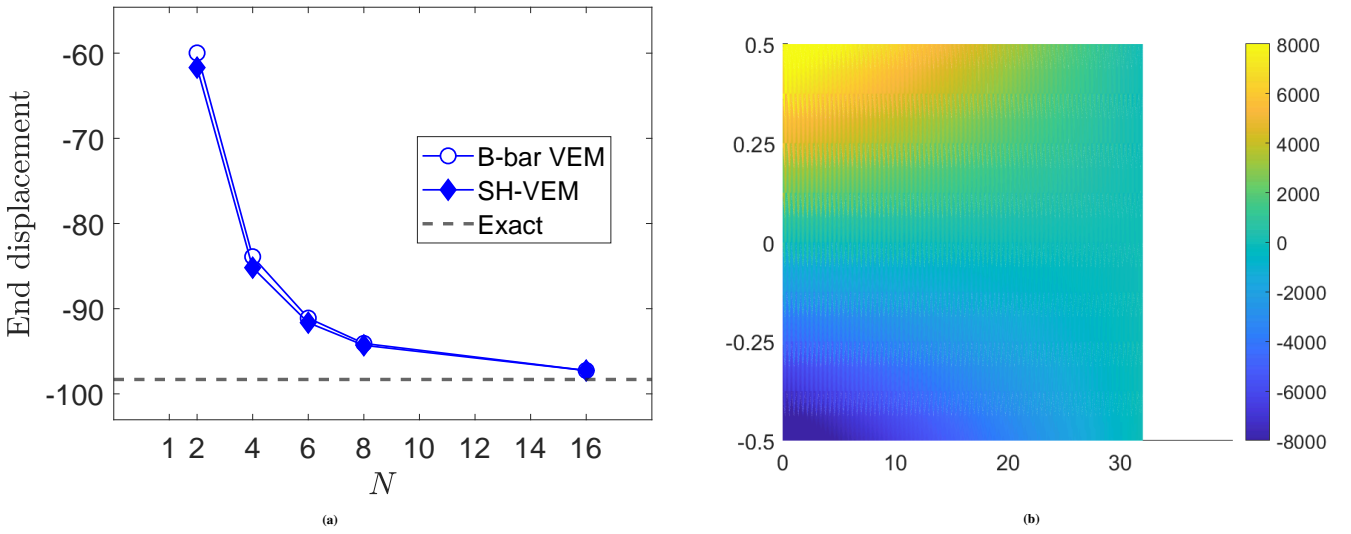


FIGURE 18 (a) Convergence of the end displacement for the cantilever beam problem. The mesh consists of $10N \times N$ quadrilaterals, where N is the number of elements along the height of the beam, (b) contour plot of hydrostatic stress for SH-VEM.

B-bar VEM and SH-VEM have comparable accuracy and convergence for the tip displacement. In addition, SH-VEM is able to produce a relatively smooth hydrostatic stress field on an unstructured mesh.

Next, the SH-VEM is now assessed for the Cook's membrane problem on nonconvex meshes. We begin with an unstructured quadrilateral mesh, and then each element is split into a convex and a nonconvex quadrilateral. A few representative meshes are shown in Figure 21. The plots of the convergence of tip displacement and the contour of the hydrostatic stress are presented in Figure 22. The plots show that even on nonconvex meshes, the convergence of the tip displacement of B-bar VEM and SH-VEM are proximal, and the contours of the hydrostatic stress for SH-VEM remains relatively smooth.

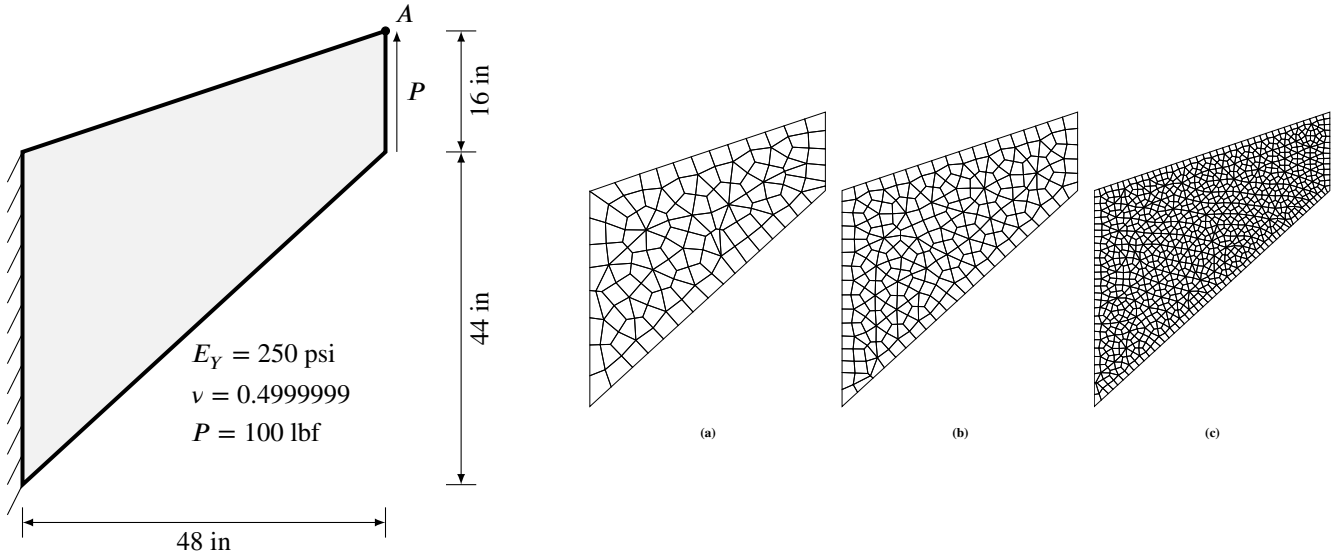


FIGURE 19 (a) Cook's membrane problem. (b), (c), (d) Unstructured quadrilateral meshes with 100 elements, 300 elements and 1000 elements, respectively.

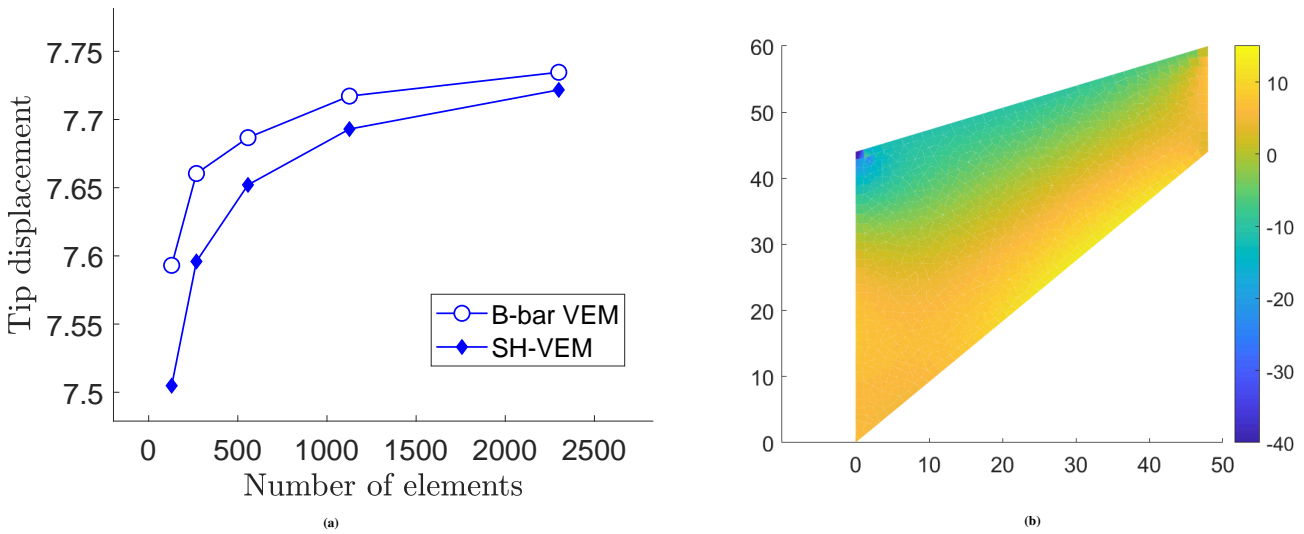


FIGURE 20 (a) Convergence of the tip displacement for Cook's membrane problem. The mesh consists of unstructured quadrilaterals. (b) Contour plot of the hydrostatic stress for SH-VEM.

5.5 | Plate with a circular hole

We consider the problem of an infinite plate with a circular hole under uniaxial tension along the x -direction.⁴⁸ The hole is traction-free, and a far-field tensile load $\sigma_0 = 1$ psi is applied. On using symmetry, we model a quarter of the plate with length $L = 5$ inch and a hole of radius $a = 1$ inch. The exact tractions are applied on the traction boundaries. The material has Young's modulus $E_Y = 2 \times 10^7$ psi and Poisson's ratio $\nu = 0.4999999$. We first test this problem on structured quadrilateral meshes; a few representative meshes are shown in Figure 23. In Figure 24, we compare the convergence results of the B-bar formulation

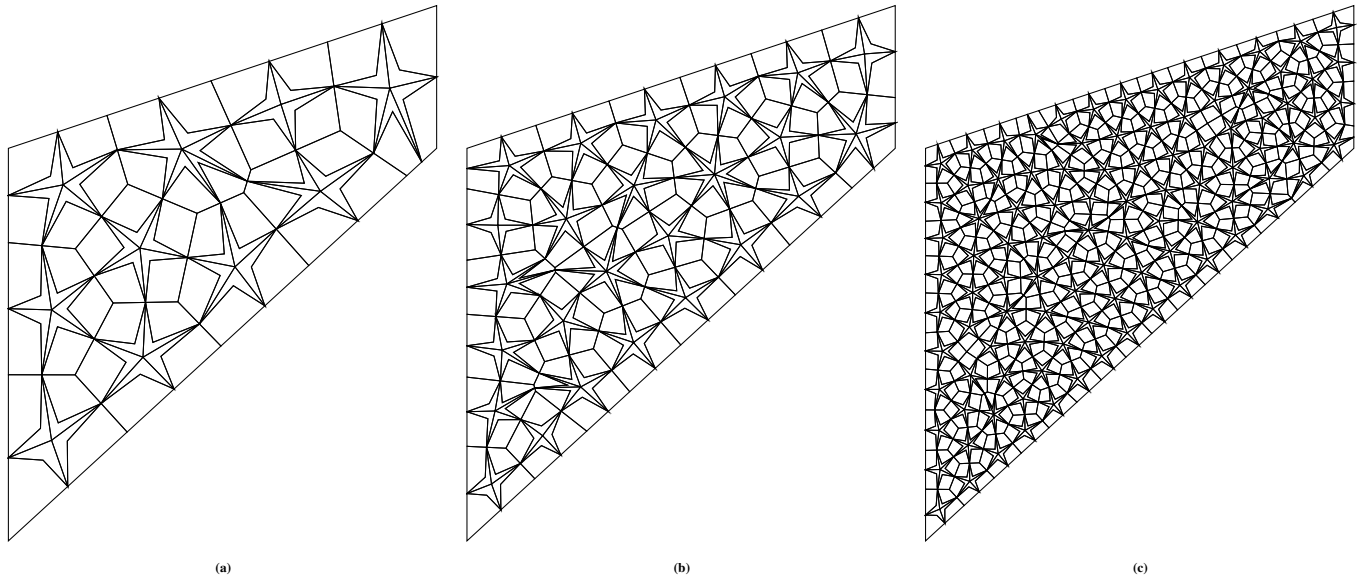


FIGURE 21 Nonconvex quadrilateral meshes for the Cook's membrane problem. (a) 100 elements, (b) 250 elements and (c) 1000 elements.

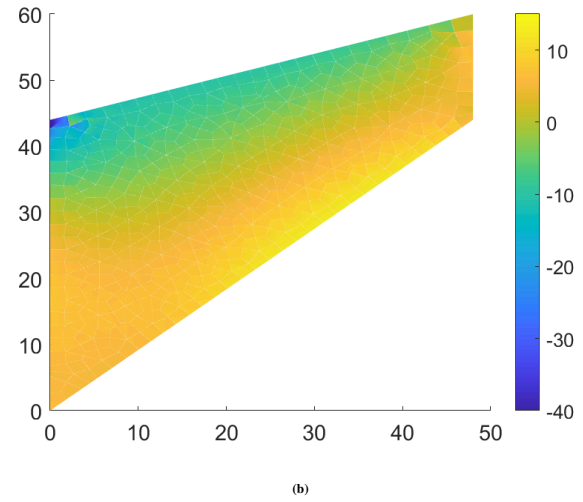
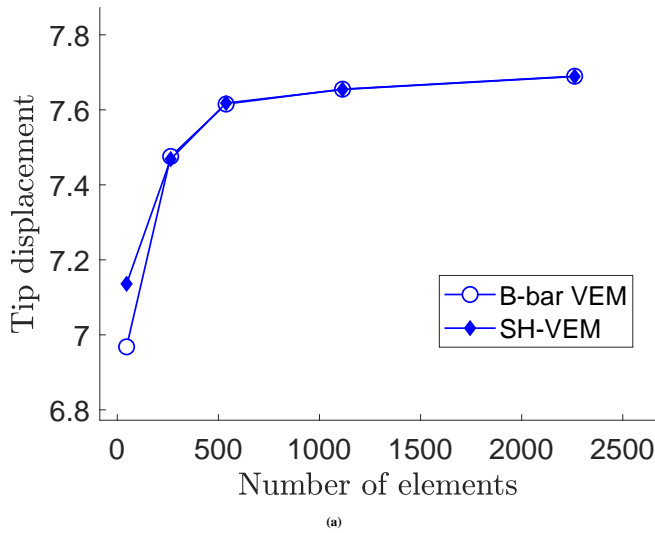


FIGURE 22 (a) Convergence of the tip displacement for Cook's membrane. The mesh consists of nonconvex quadrilaterals and (b) contour plot of the hydrostatic stress for SH-VEM.

and the SH-VEM, and find that both methods deliver optimal convergence rates. In Figure 25, we also compare the contours of the hydrostatic stress by the two methods and find that they both are smooth and have comparable accuracy.

We now consider the plate with a circular hole problem on a perturbed mesh. We start with a structured mesh, then for each internal node we perturb its location. Representative meshes are shown in Figure 26. In Figure 27, we show the convergence rates of the two methods and find that both methods retain optimal convergence on the perturbed mesh. In Figure 28, the exact

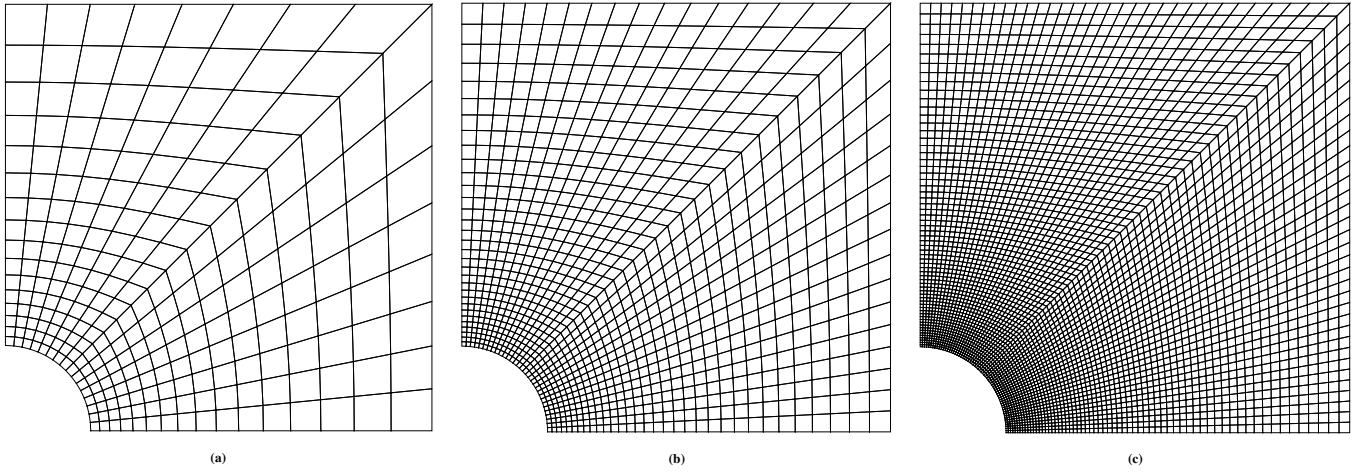


FIGURE 23 Structured quadrilateral meshes for the plate with a hole problem. (a) 256 elements, (b) 1024 elements and (c) 4096 elements.

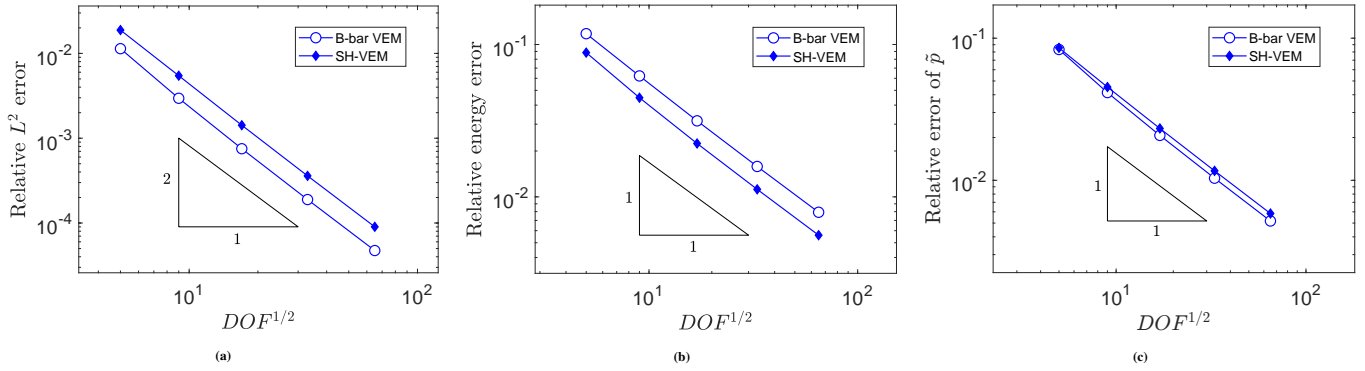


FIGURE 24 Comparison of SH-VEM and B-bar VEM for the plate with a circular hole problem on structured meshes. (a) L^2 error of displacement, (b) energy error and (c) L^2 error of the hydrostatic stress.

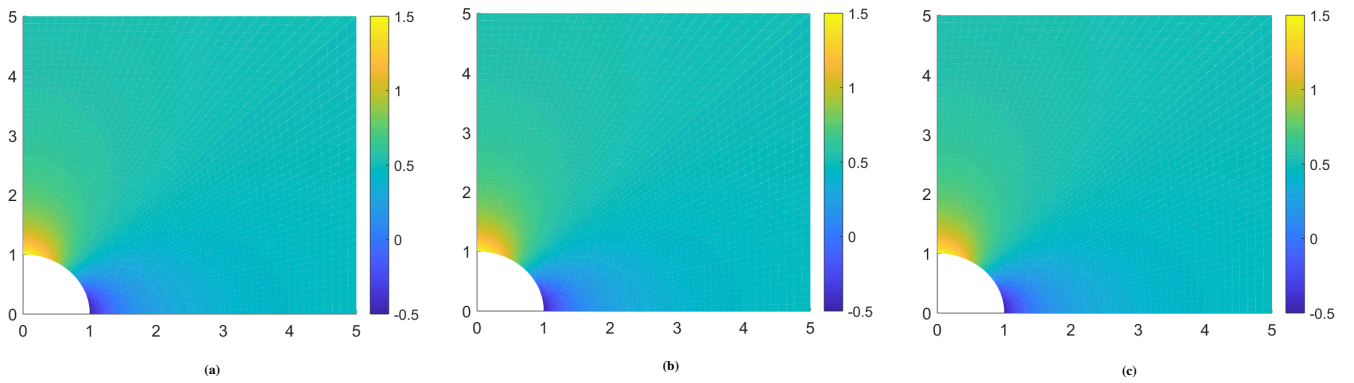


FIGURE 25 Contour plots of the hydrostatic stress on structured meshes for the plate with a circular hole problem. (a) exact solution, (b) B-bar VEM, (c) SH-VEM.

hydrostatic stress and contour plots of the error, $|\tilde{p} - \tilde{p}_h|$, are shown. The plots reveal that both methods produce relatively smooth error distributions of the hydrostatic stress field, with the B-bar VEM having smaller pointwise error than SH-VEM.

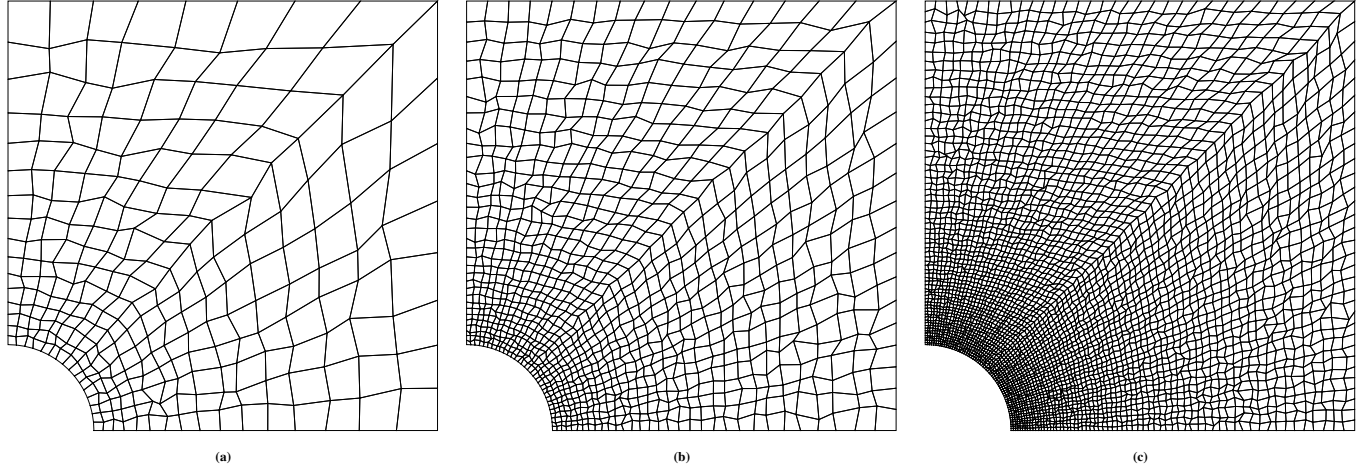


FIGURE 26 Perturbed quadrilateral meshes for the plate with a hole problem. (a) 256 elements, (b) 1024 elements and (c) 4096 elements.

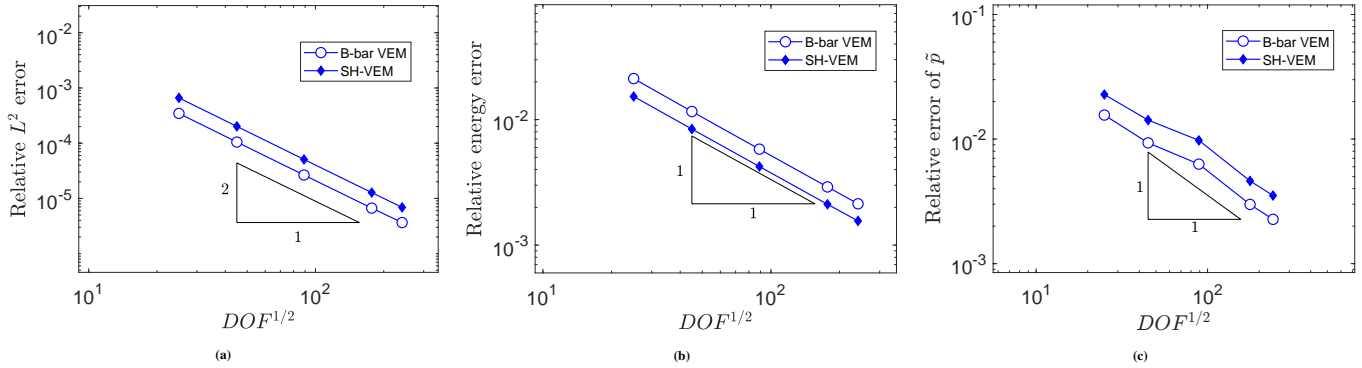


FIGURE 27 Comparison of SH-VEM and B-bar VEM for the plate with a circular hole problem on perturbed meshes. (a) L^2 error of displacement, (b) energy error and (c) L^2 error of hydrostatic stress.

5.6 | Hollow cylinder under internal pressure

We consider the problem of a hollow cylinder with inner radius $a = 1$ inch and outer radius $b = 5$ inch under internal pressure.⁴⁸ Due to symmetry, we model this problem as a quarter cylinder. A uniform pressure of $p = 10^5$ psi is applied on the inner radius, while the outer radius is kept traction-free. The material has Young's modulus $E_Y = 2 \times 10^5$ psi and Poisson's ratio $\nu = 0.4999999$. We first examine this problem on structured quadrilateral meshes; a few representative meshes are presented in Figure 29. In Figure 30, the convergence rates of B-bar VEM and SH-VEM are shown. For both methods, convergence in L^2

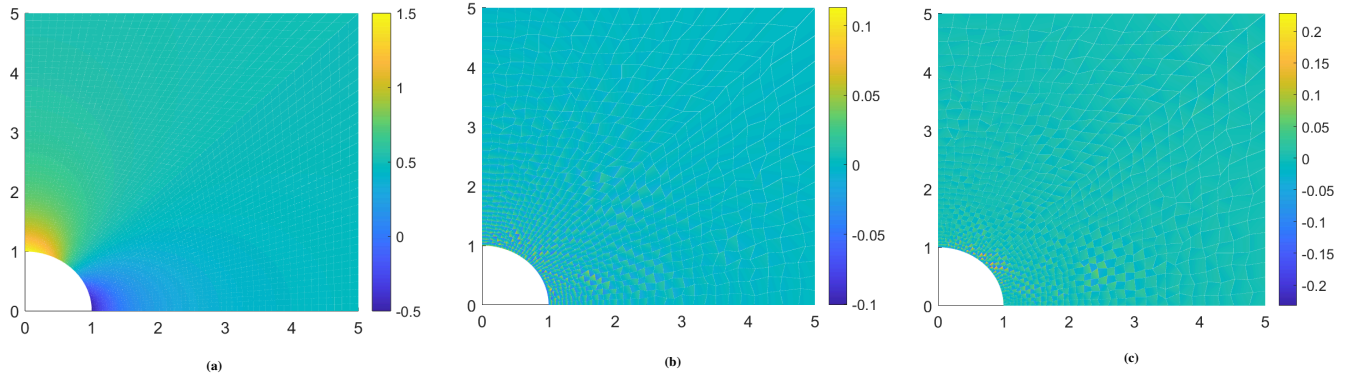


FIGURE 28 Contour plots of the hydrostatic stress for the plate with a circular hole problem. (a) exact solution, and error in the hydrostatic stress field, $|\bar{p} - \bar{p}_h|$ for (b) B-bar VEM and (c) SH-VEM.

norm and energy seminorm is optimal. The contour plots in Figure 31 show that both methods are able to reproduce the constant exact hydrostatic stress field on a uniform mesh.

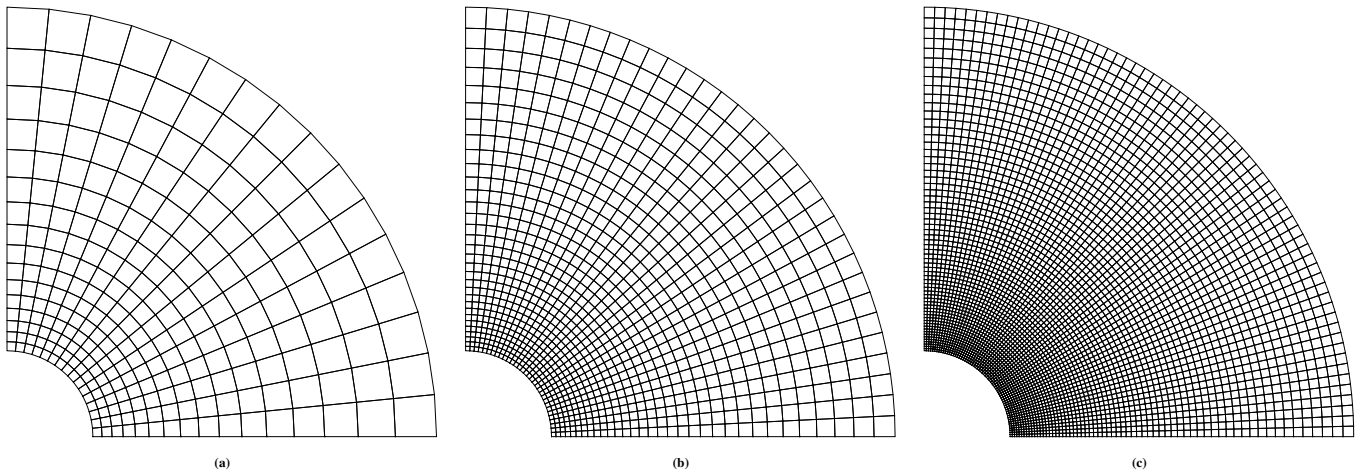


FIGURE 29 Uniform quadrilateral meshes for the hollow cylinder problem. (a) 256 elements, (b) 1024 elements and (c) 4096 elements.

Now we solve the pressurized cylinder problem on a sequence of nonconvex meshes; a few representation meshes are shown in Figure 32. Figure 33 shows that both the B-bar VEM and the SH-VEM deliver optimal convergence rates; however unlike the uniform mesh case, the hydrostatic stress field is not exactly reproduced by either method. In Figure 34, we compare the contour plots of the error in the hydrostatic stress field for the two methods. We observe that both methods are very accurate away from the inner circular boundary but produce much larger errors in its vicinity (see Figures 34b and 34d). The maximum error of the SH-VEM is 30 percent, whereas that of B-bar VEM is markedly worse at 55 percent. Compared to Figure 32c, if the nonconvex quadrilateral is distorted even more, we find from our simulations that the maximum error in the hydrostatic stress for SH-VEM increases to 35 percent, whereas the maximum error using B-bar VEM has a 10-fold increase.

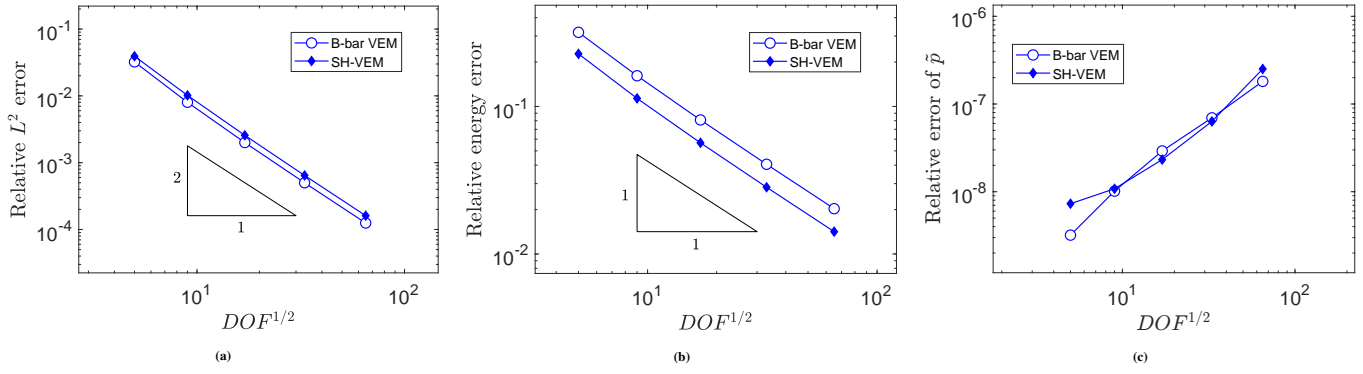


FIGURE 30 Comparison of B-bar VEM and SH-VEM for the hollow cylinder problem on structured meshes. (a) L^2 error of displacement, (b) energy error and (c) L^2 error of hydrostatic stress.

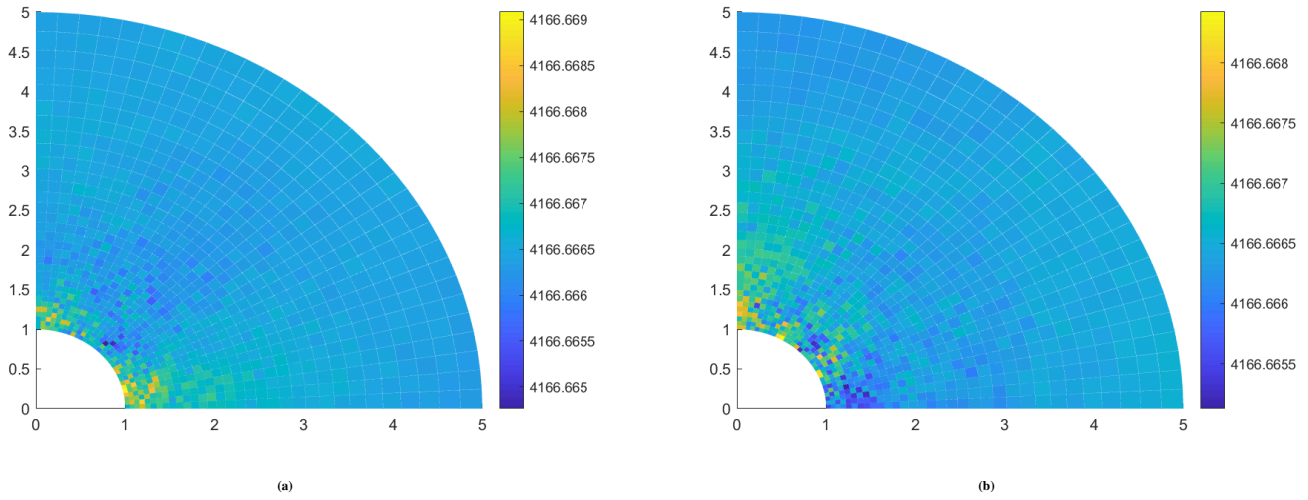


FIGURE 31 Contour plots of the hydrostatic stress field on structured meshes for the hollow pressurized cylinder problem. The exact hydrostatic stress is 4166.6666 psi. (a) B-bar VEM and (b) SH-VEM.

5.7 | Flat punch

Finally, we consider the problem of a flat punch as described in Park et al.⁶ and shown in Figure 35. The domain is the unit square and we choose $E_Y = 250$ psi and $\nu = 0.4999999$. The left, right and bottom edges are constrained in the direction normal to the edges, and the top has a constant vertical displacement of $v = -0.03$ applied on the middle third of the edge. A sequence of unstructured quadrilateral (see Figure 4) is used to solve this problem. The hydrostatic stress field from both methods are presented in Figure 36. The plots show that both methods produce relatively smooth hydrostatic stress fields of comparable accuracy. In Figure 37, plots of the trace of the strain field are shown for B-bar VEM and SH-VEM, and we find that consistent with the exact solution the numerically computed strain field is nearly traceless.

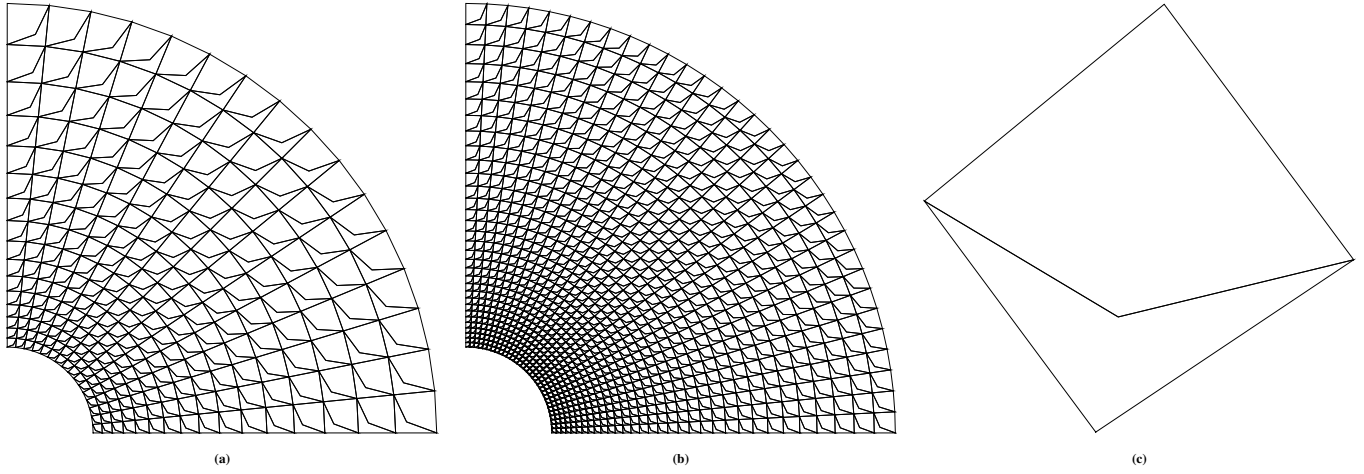


FIGURE 32 Nonconvex quadrilateral meshes for the hollow cylinder problem. (a) 512 elements, (b) 2048 elements and (c) magnification of a single element split into convex and nonconvex partitions.

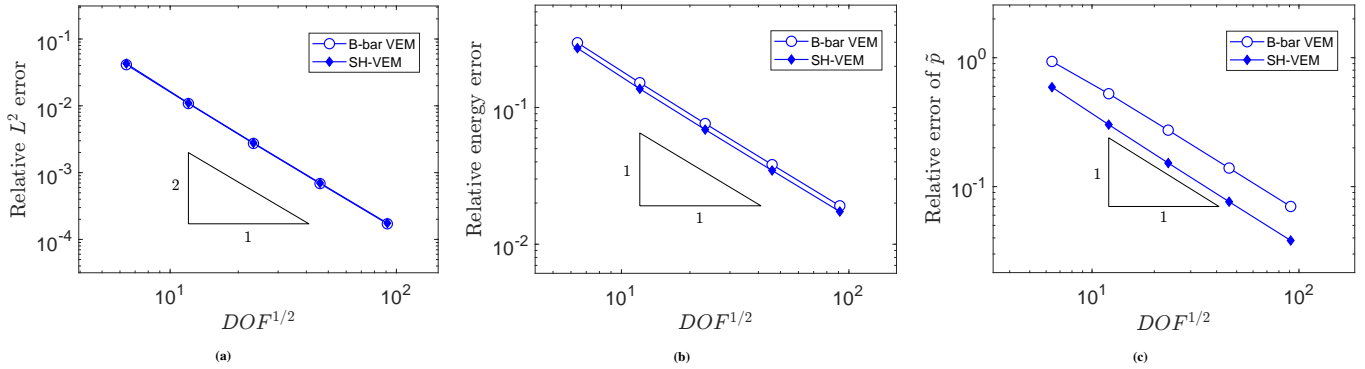


FIGURE 33 Comparison of B-bar VEM and SH-VEM for the hollow cylinder problem on nonconvex meshes. (a) L^2 error of displacement, (b) energy error and (c) L^2 error of hydrostatic stress.

6 | CONCLUSIONS

In this paper, to treat nearly-incompressible materials in linear elasticity, we departed from the commonly used assumed-strain approaches in finite element methods that rely on the Hu–Washizu three-field variational principle.⁹ Instead, we revisited the assumed stress (or stress-hybrid) formulation that use the two-field Hellinger–Reissner variational principle.¹⁶ In so doing, we proposed a stress-hybrid formulation¹⁶ of the virtual element method on quadrilateral meshes for problems in plane linear elasticity. In this approach, the Hellinger–Reissner functional is used to define weak imposition of equilibrium equations and the strain-displacement relations to determine a suitable projection operator for the stress. On each quadrilateral element, we constructed a local coordinate system^{42,43} and used a 5-term divergence-free symmetric tensor polynomial basis in the local coordinate system. The rotation matrix was then used to transform the stress ansatz to the global Cartesian coordinates so that element stiffness matrix computations could be conducted directly on the physical (distorted) element. On applying the

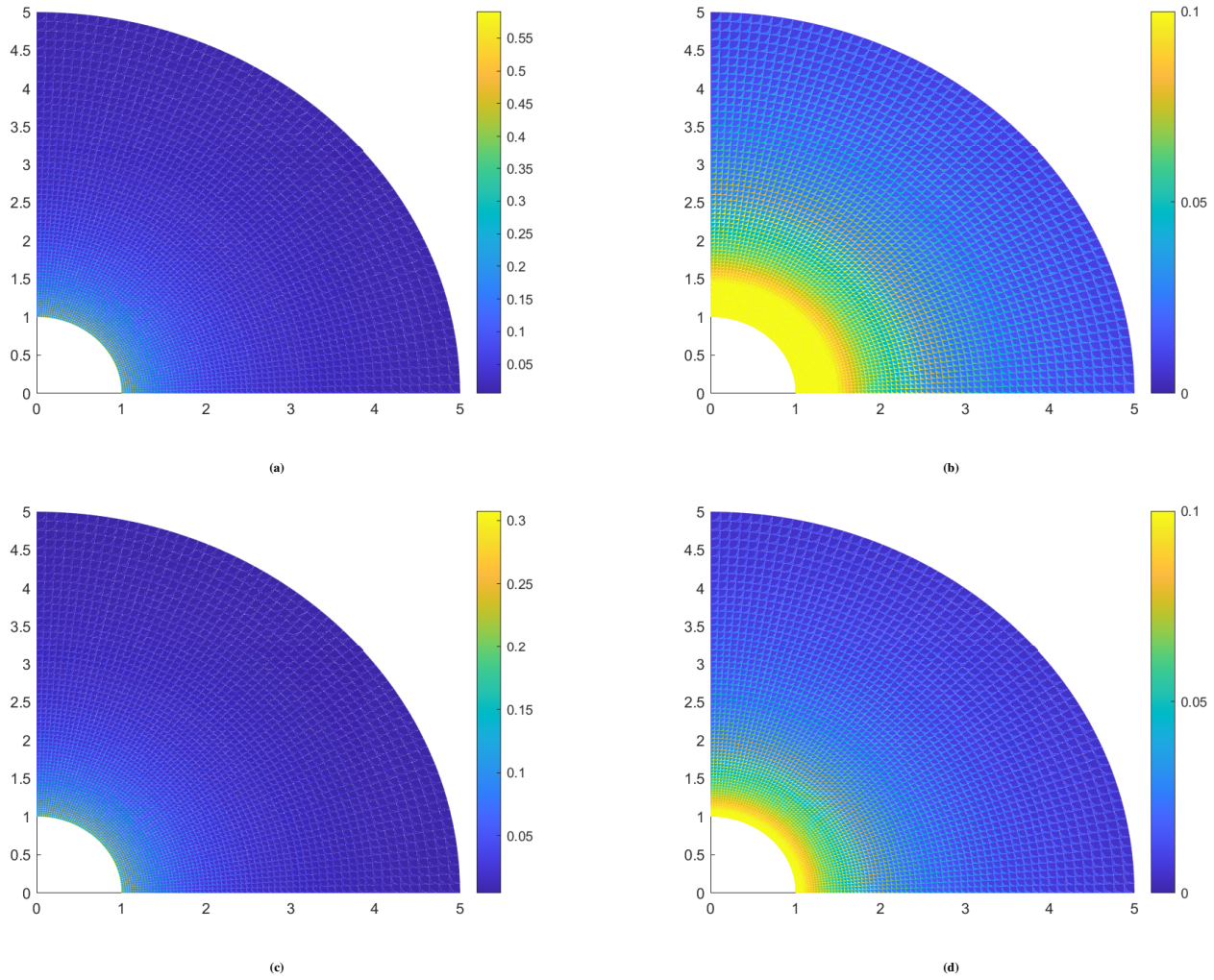


FIGURE 34 Contour plots of the relative error in the hydrostatic stress on nonconvex meshes for the hollow pressurized cylinder problem. The exact hydrostatic stress is 4166.6666 psi. (a) B-bar VEM, (b) B-bar VEM (color scale for error is between 0 and 10 percent), (c) SH-VEM and (d) SH-VEM (color scale for error is between 0 and 10 percent).

divergence theorem on each element and using the divergence-free basis, we were able to compute the matrix representation of the stress projection solely from the displacements on the boundary. This resulted in a displacement-based method that was computable using the virtual element formulation. In the Appendix, we showed that the proposed approach was equivalent to a stress-hybrid virtual element formulation that follows the recipe of Cook⁴² to transform the element stiffness matrix from local to global Cartesian coordinates. The SH-formulation was tested for stability, volumetric and shear locking, and convergence on several benchmark problems. From an element-eigenvalue analysis, we found that the proposed method was rotationally invariant and remained stable for a large class of convex and nonconvex elements without needing a stabilization term. For a manufactured test problem in the incompressible limit ($\nu \rightarrow 0.5$), we showed that the SH-VEM did not suffer from volumetric locking. From the bending of a thin beam and the bending in the Cook's membrane problem, we found that the method was not susceptible to shear locking. For a plate with a circular hole, the methods produced optimal convergence rates and smooth

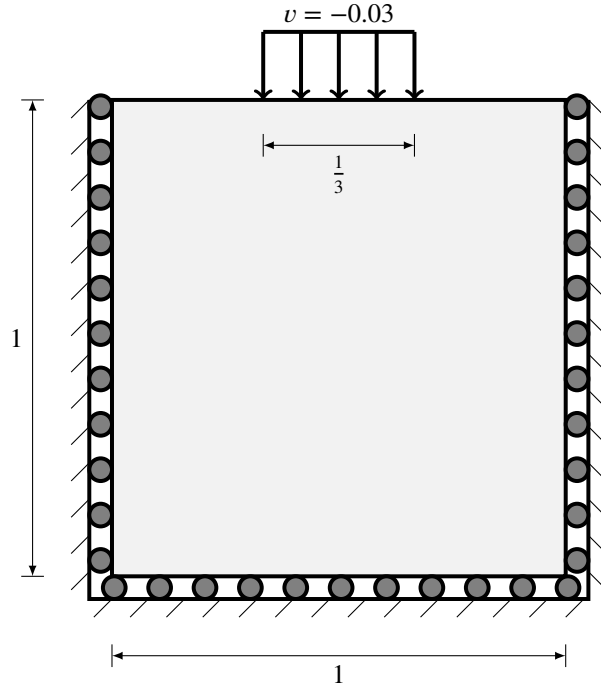


FIGURE 35 Flat punch problem.

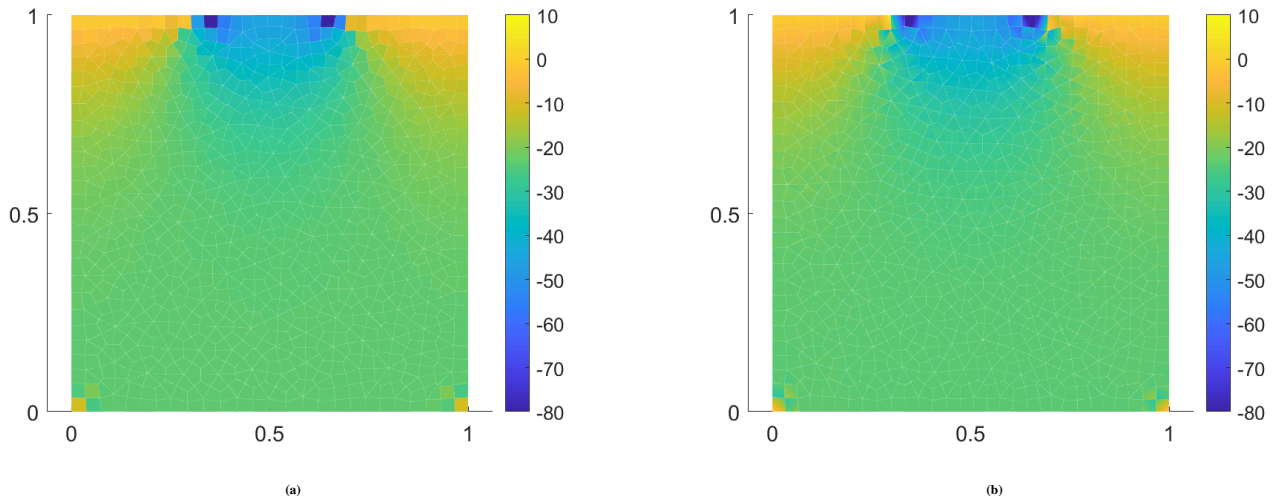


FIGURE 36 Contour plots of the hydrostatic stress on unstructured meshes for the flat punch problem. (a) B-bar VEM and (b) SH-VEM.

hydrostatic stress fields for both convex and nonconvex meshes. For the pressurized cylinder, optimal convergence rates in the L^2 norm and energy seminorm of the displacement field were realized, and both the B-bar VEM and the SH-VEM reproduced close to the exact hydrostatic stress on uniform meshes. However, it was observed that the hydrostatic stress field using the B-bar VEM and the SH-VEM on distorted *nonconvex meshes* produced larger errors, with the latter being more accurate. In the problem of a flat punch, the B-bar VEM and the SH-VEM produced relatively smooth hydrostatic stress fields that were comparable and

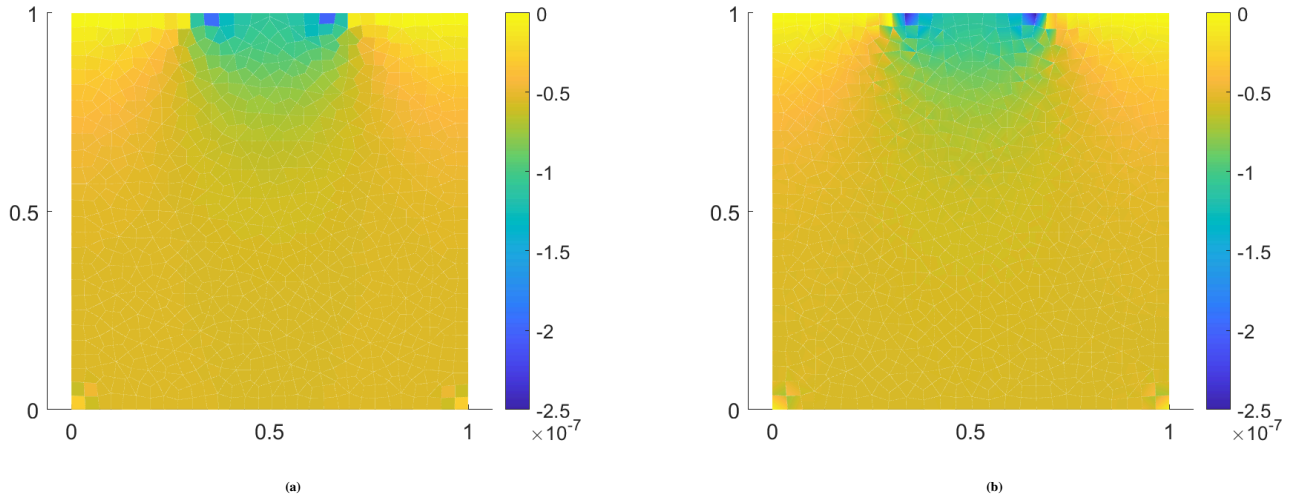


FIGURE 37 Contour plots of the trace of the strain field on unstructured meshes for the flat punch problem. (a) B-bar VEM and (b) SH-VEM.

the strain field was pointwise nearly traceless. As future work, we plan to extend the stress-hybrid virtual element method to polygonal meshes for compressible and nearly-incompressible linear elasticity.

ACKNOWLEDGEMENTS

The authors acknowledge the research support of Sandia National Laboratories to the University of California at Davis. NS is grateful to Professor Chandrashekhara Jog (Department of Mechanical Engineering, IISc Bangalore) for many helpful discussions on the stress-hybrid finite element method. These discussions in July 2022 provided the seeds to pursue the present contribution.



APPENDIX

A STRESS-HYBRID FORMULATION BASED ON COOK'S APPROACH

In this Appendix, we present an alternate formulation of the stress-hybrid virtual element method based on defining the element stiffness matrix on a rotated element as introduced by Cook.⁴² Let E' be a rotated element, and following (24), define the corresponding matrices H' and L' by

$$H' = \int_{E'} (\mathbf{P}')^T \mathbf{C}^{-1} \mathbf{P}' d\mathbf{x}', \quad L' = \int_{\partial E'} (\mathbf{P}')^T \mathbf{N}^{\partial E'} \boldsymbol{\varphi}' ds', \quad (\text{A1a})$$

where \mathbf{P}' is given in (18a) and $\boldsymbol{\varphi}'$ are the virtual element basis functions on E' . We then solve for the stress coefficients $\boldsymbol{\beta}'$ in terms of the rotated displacements using

$$\boldsymbol{\beta}' = (\mathbf{H}')^{-1} \mathbf{L}' \mathbf{d}' := \boldsymbol{\Pi}'_{\beta} \mathbf{d}'. \quad (\text{A1b})$$

The element stiffness matrix on the rotated element E' is given as

$$\mathbf{K}'_{E'} = (\boldsymbol{\Pi}'_{\beta})^T \left(\int_{E'} (\mathbf{P}')^T \mathbf{C}^{-1} \mathbf{P}' d\mathbf{x}' \right) \boldsymbol{\Pi}'_{\beta} = (\boldsymbol{\Pi}'_{\beta})^T \mathbf{H}' \boldsymbol{\Pi}'_{\beta}, \quad (\text{A2})$$

and define the rotation matrix \mathbf{R} as

$$\mathbf{R} = \begin{bmatrix} \mathbf{Q} & \mathbf{0} & \mathbf{0} & \mathbf{0} \\ \mathbf{0} & \mathbf{Q} & \mathbf{0} & \mathbf{0} \\ \mathbf{0} & \mathbf{0} & \mathbf{Q} & \mathbf{0} \\ \mathbf{0} & \mathbf{0} & \mathbf{0} & \mathbf{Q} \end{bmatrix}, \quad (\text{A3})$$

where \mathbf{Q} is given in (17), and $\mathbf{0}$ is the 2×2 zero matrix. Then the element stiffness matrix in Cook's formulation on the original element E is recovered by:

$$\mathbf{K}_E^C = \mathbf{R}^T \mathbf{K}'_{E'} \mathbf{R}. \quad (\text{A4})$$

Now, on applying (A1b) and simplifying, we write the element stiffness matrix as

$$\mathbf{K}_E^C = \mathbf{R}^T ((\mathbf{H}')^{-1} \mathbf{L}')^T \mathbf{H}' (\mathbf{H}')^{-1} \mathbf{L}' \mathbf{R} = (\mathbf{L}' \mathbf{R})^T (\mathbf{H}')^{-1} (\mathbf{L}' \mathbf{R}).$$

We now show that the SH-VEM using the basis \mathbf{P}^* in (20) is identical to Cook's formulation, i.e., $\mathbf{K}_E^* = \mathbf{K}_E^C$.

Proof. On expanding the element stiffness matrix of the SH-VEM given in (27) and simplifying, we get

$$\mathbf{K}_E^* = \boldsymbol{\Pi}_{\beta}^T \mathbf{H}^* \boldsymbol{\Pi}_{\beta} = ((\mathbf{H}^*)^{-1} \mathbf{L}^*)^T \mathbf{H}^* (\mathbf{H}^*)^{-1} \mathbf{L}^* = (\mathbf{L}^*)^T (\mathbf{H}^*)^{-1} \mathbf{L}^*.$$

We first examine the matrix \mathbf{H}^* . From (24a), we have

$$\mathbf{H}^* = \int_E (\mathbf{P}^*)^T \mathbf{C}^{-1} \mathbf{P}^* d\mathbf{x},$$

and after multiplying out the matrices and using an equivalent tensor representation, we write the components of \mathbf{H}^* as

$$H_{ij}^* = \int_E \mathbf{P}_i^* : \mathbb{C}^{-1} : \mathbf{P}_j^* d\mathbf{x},$$

where \mathbf{P}_i^* is the tensor representation of the i -th column of \mathbf{P}^* . Using (19), we rewrite this integral in terms of the rotated basis \mathbf{P}'_i , that is

$$\mathbf{H}_{ij}^* = \int_{E'} \mathbf{Q}^T \mathbf{P}'_i \mathbf{Q} : \mathbb{C}^{-1} : \mathbf{Q}^T \mathbf{P}'_j \mathbf{Q} d\mathbf{x}'.$$

It can be shown that for an isotropic material modulli tensor \mathbb{C} , that

$$\mathbf{Q}^T \mathbf{P}'_i \mathbf{Q} : \mathbb{C}^{-1} : \mathbf{Q}^T \mathbf{P}'_j \mathbf{Q} = \mathbf{P}'_i : \mathbf{Q}^T \mathbf{Q}^T \mathbb{C}^{-1} \mathbf{Q} \mathbf{Q} : \mathbf{P}'_j = \mathbf{P}'_i : \mathbb{C}^{-1} : \mathbf{P}'_j.$$

Therefore, we now have for all $i, j = 1, 2, \dots, 5$:

$$\mathbf{H}_{ij}^* = \int_{E'} \mathbf{P}'_i : \mathbb{C}^{-1} : \mathbf{P}'_j d\mathbf{x}' = \mathbf{H}'_{ij}. \quad (\text{A6})$$

Next, we examine the matrix \mathbf{L}^* . From (24a), we have

$$\mathbf{L}^* = \int_{\partial E} (\mathbf{P}^*)^T \mathbf{N}^{\partial E} \boldsymbol{\varphi} ds,$$

After converting to an equivalent tensor representation, we write the components of \mathbf{L}^* as:

$$L_{ij}^* = \int_{\partial E} (\mathbf{P}_i^* \cdot \mathbf{n}) \cdot \boldsymbol{\varphi}_j ds.$$

Since $\boldsymbol{\varphi}_j$ and $\boldsymbol{\varphi}'_j$ are both piecewise affine functions on ∂E and $\partial E'$, respectively, it can be shown that the integration of $\boldsymbol{\varphi}_j$ along the boundary of an element E is equivalent to integrating $\boldsymbol{\varphi}'_j$ along the boundary of the rotated element E' . That is, for any vector field \mathbf{f} , we have

$$\int_{\partial E} \mathbf{f}(\mathbf{x}) \cdot \boldsymbol{\varphi}_j ds = \int_{\partial E'} \mathbf{f}(\mathbf{x}(\mathbf{x}')) \cdot \boldsymbol{\varphi}'_j ds'.$$

With this, we rewrite L_{ij}^* in the rotated coordinates as

$$L_{ij}^* = \int_{\partial E} (\mathbf{P}_i^* \cdot \mathbf{n}) \cdot \boldsymbol{\varphi}_j ds = \int_{\partial E'} (\mathbf{Q}^T \mathbf{P}'_i \mathbf{Q} \cdot \mathbf{Q}^T \mathbf{n}') \cdot \boldsymbol{\varphi}'_j ds' = \int_{\partial E'} (\mathbf{Q}^T \mathbf{P}'_i \cdot \mathbf{n}') \cdot \boldsymbol{\varphi}'_j ds'.$$

If we take the basis functions in the standard order $\boldsymbol{\varphi}'_{2j-1} = (\phi'_j, 0)^T$ and $\boldsymbol{\varphi}'_{2j} = (0, \phi'_j)^T$, then we can simplify L_{ij}^* as:

$$\begin{aligned} L_{i2j-1}^* &= c \int_{\partial E'} ((\mathbf{P}'_i)_{11} \mathbf{n}'_1 + (\mathbf{P}'_i)_{12} \mathbf{n}'_2) \phi'_j ds' - s \int_{\partial E'} ((\mathbf{P}'_i)_{12} \mathbf{n}'_1 + (\mathbf{P}'_i)_{22} \mathbf{n}'_2) \phi'_j ds' = c L'_{i2j-1} - s L'_{i2j} \\ L_{i2j}^* &= s \int_{\partial E'} ((\mathbf{P}'_i)_{11} \mathbf{n}'_1 + (\mathbf{P}'_i)_{12} \mathbf{n}'_2) \phi'_j ds' + c \int_{\partial E'} ((\mathbf{P}'_i)_{12} \mathbf{n}'_1 + (\mathbf{P}'_i)_{22} \mathbf{n}'_2) \phi'_j ds' = s L'_{i2j-1} + c L'_{i2j}, \end{aligned}$$

where c and s given in (17). On multiplying out the matrix $\mathbf{L}'\mathbf{R}$, it can be shown that

$$(\mathbf{L}'\mathbf{R})_{i2j-1} = c\mathbf{L}'_{i2j-1} - s\mathbf{L}'_{i2j}$$

$$(\mathbf{L}'\mathbf{R})_{i2j} = s\mathbf{L}'_{i2j-1} + c\mathbf{L}'_{i2j},$$

and therefore for all $i = 1, 2, \dots, 5$ and $j = 1, 2, \dots, 4$, we have

$$\mathbf{L}^*_{i2j-1} = c\mathbf{L}'_{i2j-1} - s\mathbf{L}'_{i2j} = (\mathbf{L}'\mathbf{R})_{i2j-1} \quad (\text{A7a})$$

$$\mathbf{L}^*_{i2j} = s\mathbf{L}'_{i2j-1} + c\mathbf{L}'_{i2j} = (\mathbf{L}'\mathbf{R})_{i2j}. \quad (\text{A7b})$$

From (A6) and (A7), we obtain $\mathbf{H}^* = \mathbf{H}'$ and $\mathbf{L}^* = \mathbf{L}'\mathbf{R}$. On substituting these in (A5) and using (A4) leads us to the desired result:

$$\mathbf{K}_E^* = (\mathbf{L}^*)^T (\mathbf{H}^*)^{-1} \mathbf{L}^* = (\mathbf{L}'\mathbf{R})^T (\mathbf{H}')^{-1} (\mathbf{L}'\mathbf{R}) = \mathbf{K}_E^C. \quad \square$$

References

1. Ainsworth M, Parker C. Unlocking the secrets of locking: Finite element analysis in planar linear elasticity. *Comput Methods Appl Mech Eng* 2022; 395: 115034.
2. Beirão da Veiga L, Brezzi F, Cangiani A, Manzini G, Marini LD, Russo A. Basic principles of virtual element methods. *Math Models Methods Appl Sci* 2013; 23: 119–214.
3. Beirão da Veiga L, Brezzi F, Marini D. Virtual elements for linear elasticity problems. *SIAM J Numer Anal* 2013; 51(2): 794–812.
4. Artioli E, de Miranda S, Lovadina C, Patruno L. A family of virtual element methods for plane elasticity problems based on the Hellinger–Reissner principle. *Comput Methods Appl Mech Eng* 2018; 340: 978–999.
5. Cáceres E, Gatica GN, Sequeira FA. A mixed virtual element method for a pseudostress-based formulation of linear elasticity. *Appl Numer Math* 2019; 135: 423–442.
6. Park K, Chi H, Paulino G. B-bar virtual element method for nearly incompressible and compressible materials. *Meccanica* 2020; 56: 1423–1439.
7. Artioli, Edoardo, de Miranda, Stefano, Lovadina, Carlo, Patruno, Luca. A dual hybrid virtual element method for plane elasticity problems. *ESAIM: M2AN* 2020; 54(5): 1725–1750.

8. Dassi F, Lovadina C, Visinoni M. Hybridization of the virtual element method for linear elasticity problems. *Math Models Methods Appl Sci* 2021; 31(14): 2979–3008.
9. Simo JC, Hughes TJR. On the Variational Foundations of Assumed Strain Methods. *J Appl Mech* 1986; 53(1): 51–54.
10. Simo JC, Rifai MS. A class of mixed assumed strain methods and the method of incompatible modes. *Int J Numer Methods Eng* 1990; 29(8): 1595–1638.
11. Berrone S, Borio A, Marcon F. Lowest order stabilization free Virtual Element Method for the Poisson equation. arXiv preprint: 2103.16896; 2021.
12. D’Altri AM, de Miranda S, Patruno L, Sacco E. An enhanced VEM formulation for plane elasticity. *Comput Methods Appl Mech Eng* 2021; 376: 113663.
13. Chen A, Sukumar N. Stabilization-free virtual element method for plane elasticity. *Comput Math Applications* 2023; 138: 88–105.
14. Chen A, Sukumar N. Stabilization-free serendipity virtual element method for plane elasticity. *Comput Methods Appl Mech Eng* 2023; 404: 115784.
15. Lamperti A, Cremonesi M, Perego U, Russo A, Lovadina C. A Hu–Washizu variational approach to self-stabilized virtual elements: 2D linear elastostatics. *Comput Mech* 2023. doi: <https://doi.org/10.1007/s00466-023-02282-2>
16. Pian THH, Sumihara K. Rational approach for assumed stress finite elements. *Int J Numer Methods Eng* 1984; 20(9): 1685–1695.
17. Pian THH, Wu CC. A rational approach for choosing stress terms for hybrid finite element formulations. *Int J Numer Methods Eng* 1988; 26(10): 2331–2343.
18. Wilson EL, Taylor RL, Doherty WP, Ghaboussi J. Incompatible displacement models. In: Fenves SJ, Perrone N, Robinson AR, Schnobrich WC., eds. *Numerical and Computer Methods in Structural Mechanics* Elsevier. 1973 (pp. 43–57).
19. Pian THH, Tong P. Relations between incompatible displacement model and hybrid stress model. *Int J Numer Methods Eng* 1986; 22(1): 173–181.
20. Yeo ST, Lee BC. Equivalence between enhanced assumed strain method and assumed stress hybrid method based on the Hellinger–Reissner principle. *Int J Numer Methods Eng* 1996; 39(18): 3083–3099.
21. Stolarski H, Belytschko T. Limitation principles for mixed finite elements based on the Hu–Washizu variational formulation. *Comput Methods Appl Mech Eng* 1987; 60(2): 195–216.

22. Belytschko T, Bindeman L. Assumed strain stabilization of the 4-node quadrilateral with 1-point quadrature for nonlinear problems. *Comput Methods Appl Mech Eng* 1991; 88(3): 311–340.
23. Barlow J. A different view of the assumed stress hybrid method. *Int J Numer Methods Eng* 1986; 22(1): 11–16.
24. Punch E, Atluri S. Development and testing of stable, invariant, isoparametric curvilinear 2- and 3-D hybrid-stress elements. *Comput Methods Appl Mech Eng* 1984; 47(3): 331–356.
25. Lee SW, Rhiu JJ. A new efficient approach to the formulation of mixed finite element models for structural analysis. *Int J Numer Methods Eng* 1986; 23(9): 1629–1641.
26. Spilker RL. Improved hybrid-stress axisymmetric elements including behaviour for nearly incompressible materials. *Int J Numer Methods Eng* 1981; 17(4): 483–501.
27. Xie X, Zhou T. Accurate 4-node quadrilateral elements with a new version of energy-compatible stress mode. *Commun Numer Meth En* 2008; 24(2): 125–139.
28. Xie X, Zhou T. Optimization of stress modes by energy compatibility for 4-node hybrid quadrilaterals. *Int J Numer Methods Eng* 2004; 59(2): 293–313.
29. Cen S, Fu XR, Zhou MJ. 8- and 12-node plane hybrid stress-function elements immune to severely distorted mesh containing elements with concave shapes. *Comput Methods Appl Mech Eng* 2011; 200(29): 2321–2336.
30. Jog CS. Improved hybrid elements for structural analysis. *Mech Mater* 2010; 5: 507–528.
31. Jog CS. A 27-node hybrid brick and a 21-node hybrid wedge element for structural analysis. *Finite Elem Anal Des* 2005; 41(11): 1209–1232.
32. Xue WM, Karlovitz L, Atluri S. On the existence and stability conditions for mixed-hybrid finite element solutions based on Reissner's variational principle. *Int J Solids Struct* 1985; 21(1): 97–116.
33. Zhou T, Xie X. A unified analysis for stress/strain hybrid methods of high performance. *Comput Methods Appl Mech Eng* 2002; 191(41): 4619–4640.
34. Yu G, Xie X, Carstensen C. Uniform convergence and a posteriori error estimation for assumed stress hybrid finite element methods. *Comput Methods Appl Mech Eng* 2011; 200(29): 2421–2433.
35. Simo JC, Fox DD, Rifai MS. On a stress resultant geometrically exact shell model. Part II: The linear theory; Computational aspects. *Comput Methods Appl Mech Eng* 1989; 73(1): 53–92.

36. Simo JC, Kennedy JG, Taylor RL. Complementary mixed finite element formulations for elastoplasticity. *Comput Methods Appl Mech Eng* 1989; 74(2): 177–206.
37. Jog CS, Kelkar PP. Non-linear analysis of structures using high performance hybrid elements. *Int J Numer Methods Eng* 2006; 68(4): 473–501.
38. Jog CS, Motamarri P. An energy-momentum conserving algorithm for nonlinear transient analysis within the framework of hybrid elements. *J Mech Mater Struct* 2009; 4: 157–186.
39. Jog CS, Bayadi R. Stress and strain-driven algorithmic formulations for finite strain viscoplasticity for hybrid and standard finite elements. *Int J Numer Methods Eng* 2009; 2009: 773–816.
40. Jog CS, Gautam GSJ. A monolithic hybrid finite element strategy for nonlinear thermoelasticity. *Int J Numer Methods Eng* 2017; 112(1): 26–57.
41. Agrawal M, Nandy A, Jog CS. A hybrid finite element formulation for large-deformation contact mechanics. *Comput Methods Appl Mech Eng* 2019; 356: 407–434.
42. Cook RD. Improved two-dimensional finite element. *J Struct Div-ASCE* 1974; 100(9): 1851–1863.
43. Cook RD. Avoidance of parasitic shear in plane element. *J Struct Div-ASCE* 1975; 101(6): 1239–1253.
44. Ahmad B, Alsaedi A, Brezzi F, Marini LD, Russo A. Equivalent projectors for virtual element methods. *Comput Math Applications* 2013; 66: 376–391.
45. Beirão da Veiga L, Brezzi F, Marini LD, Russo A. The hitchhiker’s guide to the virtual element method. *Math Models Methods Appl Sci* 2014; 24(8): 1541–1573.
46. Piltner R, Taylor RL. A quadrilateral mixed finite element with two enhanced strain modes. *Int J Numer Methods Eng* 1995; 38(11): 1783–1808.
47. Chin EB, Sukumar N. Scaled boundary cubature scheme for numerical integration over planar regions with affine and curved boundaries. *Comput Methods Appl Mech Eng* 2021; 380: 113796.
48. Timoshenko SP, Goodier JN. *Theory of Elasticity*. New York: McGraw-Hill. third ed. 1970.
49. MacNeal RH, Harder RL. A proposed standard set of problems to test finite element accuracy. *Finite Elem Anal Des* 1985; 1(1): 3–20.